Final Degree Thesis

Grau en Enginyeria en Vehicles Aeroespacials (GREVA)

Study: Numerical model of the trajectory of meteoroids

Report

Author: Oriol Cayón Domingo

Director: Manel Soria

Co-director: Jordi Llorca

Convocation: January 15, 2020

UNIVERSITAT POLITÈCNICA DE CATALUNYA
BARCELONATECH

Escola Superior d'Enginyeries Industrial, Aeroespacial i Audiovisual de Terrassa

Statement of honor

I declare that, the work in this Degree Thesis is completely my own work, no part of this Degree Thesis is taken from other people's work without giving them credit and all references have been clearly cited.

I understand that an infringement of this declaration leaves me subject to the foreseen disciplinary actions by The Universitat Politècnica de Catalunya - BarcelonaTECH.

Signature

Study: Numerical model of the trajectory of meteoroids

Oriol Cayón Domingo

January 15, 2020

Abstract

Meteoroids that enter the earth's atmosphere and lighten up due to the collision with the air particles. In this study, a numerical model to simulate their trajectory through the Earth's atmosphere has been developed.

The code is able to determine the points of impact of the meteorite fragments with the ground and calculate the heliocentric orbit that the body followed before entering the Earth's gravitational field. The model starts from the inputs of initial position, velocity and mass of the meteor and calculates the trajectory by integrating the acceleration and loss of mass equations. These equations include the multiple physical phenomena that the body undergoes during its interaction with the atmosphere, taking into account the loss of mass, the drag force, the gravity, the fragmentation and the wind conditions.

The model has been applied to the fall of the Hamburg meteorite, recovered in 2018 and whose properties and initial conditions have been approximated thanks to the multiple recordings of the fall. To complete the results, a sensitivity study has been carried out, from which the most determining aspects of the model are found.

Table of contents

List of Figures

List of Tables

Nomenclature

α	Strength scaling parameter
Ω	Right ascension of the ascending node
ω	Argument of the perigee
Ω_E	Earth's rotation velocity
ρ_a	Atmospheric density
ρ_m	Density of the meteoroid
σ	Ablation coefficient
θ	True anomaly
$\vec{r}$	Position vector of the meteoroid
$\vec{v}$	Velocity vector of the meteoroid
a_F	Acceleration in an inertial coordinate system
a_M	Acceleration in a non-inertial coordinate system
A_s	Dimensionless shape factor
C_D	Drag coefficient
F_g	Gravitational force
K	Shape density coefficient / strength of the meteoroid
K_n	Knudsen number
m	Mass of the meteoroid
M_T	Mass of the Earth

S	Cross sectional area of the meteoroid
V_T	Lateral velocity
a	Semi-major axis of the orbit
e	Eccentricity of the orbit
ECEF	Earth Centered, Earth Fixed
ECI	Earth Centered Inertial frame
ENU	Local East, North, Up frame
G	Newton's gravitational constant
h	Specific angular momentum
i	Inclination of the orbit

1 Introduction

As a meteoroid enters the Earth's atmosphere at hypersonic speeds, multiple phenomena occur due to the interaction between the air and the body. The fact that neither the structure nor the composition of meteorites is known, coupled with the high velocities at which the fall occurs, greatly complicates the modelling of these phenomena.

The model presented in this study attempts to model all these events and to present as accurate an approximation as possible of the meteorite impact point and its heliocentric orbit.

1.1 Aim

The aim of this project is to create a numerical model that calculates the trajectory of meteoroids entering the Earth atmosphere. The goal is to create a program that is able to approximate the position where a meteoroid hits the ground and the heliocentric orbit of the meteoroid before crossing paths with the Earth.

1.2 Scope

The numerical model of the meteor trajectory developed in this project shall incorporate:

- Gravity model.
- Atmospheric wind model.
- Atmospheric density model.
- Ablation model.
- Fragmentation model.
- Drag force model.
- Integration function of the trajectory, both forwards and backwards in time.
- Study of sensitivity of certain key variables.

All of these concepts are considered in the project in order to calculate:

- The trajectory of the meteoroid.
- The coordinates and velocity of the meteor impact with the Earth's surface.
- The total disintegration of the meteoroid.
- The fragmentation points.
- The heliocentric orbit of the meteoroid before entering the Earth's atmosphere.

1.3 Requirements

- The numerical code shall be able to calculate the heliocentric orbit of a meteoroid.
- The numerical code shall be able to calculate the impact coordinates of the meteorite fragments with the ground.
- The numerical code shall stop if the mass of the meteoroid is zero or if the meteor reaches the ground.
- The numerical code shall take into account all the physical concepts described in the scope.

1.4 Justification

The purpose of this project is to develop a model able to calculate the impact point of meteoroids entering the Earth's atmosphere and determine it's initial orbit revolving around the sun.

The bodies that survive the passage through the atmosphere are also referred to as meteorites. Meteorites are really important because they hold a record of the history of our solar system that goes back as far as 4.6 billion years. By studying meteorites, we can learn details of how our solar system evolved into today's Sun and planets, and how meteorite impacts could affect our future [1]. Some of the fields studied by scientists who work with meteorites are:

- Stellar evolution: some meteorites contain dust that dates back to before the creation of the solar system, providing information on the formation and evolution of stars.
- Composition of the planets: meteorites from asteroids and other planets allow to study the creation and composition of the planets of the Solar System.
- Origin of the Solar System: some meteorites contain solid material dating from the start of the creation of the Solar System. These meteorites offer a view of the conditions at that time.
- Geologic history of Earth and the Moon: craters made from large meteorites have shaped the Earth and the Moon. Today, it is believed that the Moon was made through the impact of a huge meteorite with the Earth.
- History of life: some meteorites have brought over the years components necessary for life, such as amino acids and formic acid. Many scientists believe water also comes from comets and carbonaceous meteorites [2].

Even though meteorites are equally distributed throughout the Earth, the majority of them have been recovered near highly populated areas. That is why most of them have been recovered thanks to the eyewitnesses or because of the crater they leave on the ground. A very small number of these falls has been recorded by ground cameras and then recovered thanks to the calculation of the impact point. There are lots of stochastic and unknown factors, such as the fragmentation or the composition of the body, that difficult the modeling of the trajectory.

Even though the number of photographic recordings of meteors is growing every year, the number of recorded meteorites does not correspond to the number of meteorites found. In many cases the modeled trajectory differs from the reality by several kilometers, which makes the search very laborious to the point that many photographed meteorite falls have not yet been found.

There are multiple published papers presenting models for the calculation of the meteoroid trajectory, but the majority focus on different aspects of the meteoroid physics (such as energy deposition [3], impact energy or fragmentation [4]), rather than being entirely devoted to the trajectory calculation, and use the trajectory model as a tool for other purposes. As a consequence these tools don't offer the precision required for the recovery of meteorite based

on the calculation of the impact point.

Unlike other articles, this work is exclusively centered on the calculation of the trajectory of meteoroids entering the Earth's atmosphere and the determination of its heliocentric orbit, which is still an open matter in meteoritic science. This project includes multiple concepts and theories that have been studied individually and puts them together in the same code with the aim of creating a model that is as accurate and precise as possible in its goal.

2 Meteor Overview

Bodies of space that intercept the Earth's atmosphere and are large enough produce light during part of the fall. This phenomenon is traditionally referred to as a meteor. This term is also used for the solid piece. To avoid confusion, in this project the solid particle will be called meteoroid and the whole phenomena meteor. Finally, a meteoroid that survives the passage through the Earth's atmosphere and reaches the surface of the Earth is called meteorite.

Following the IAU (International Astronomical Union) definition, for a body to be considered a meteoroid, it must be of natural origin and be roughly the size of between 30 micrometers and 1 meter [5].

Meteoroids can have very different shapes, sizes and compositions depending on its origin. Some of the meteoroids are related to comets as shower meteors derived from meteoroid streams, some of them are related to asteroids and some of them come from the process of formation of larger planetary bodies or as the disintegration of a cometary body that occasionally reaches the inner solar system [6].

2.1 Meteoroids

Most of the knowledge we know from meteoroids comes from the short interval of time where the meteoroid is shedding light. As mentioned above this phenomenon is often referred as meteor, although for great sizes and velocities, where the luminosity is greater, it is also known as a meteoric fireball and ultimately as a bolide.

The point in the heavens from which a shower of meteors seems to proceed is called the radiant. Meteoroids with similar parallel trails belong to the same meteor shower and radiate from the same point in the sky, and come from the same meteoroid stream. Meteoroids that do not belong to any shower are called sporadic meteors[7].

The velocities in which meteoroids enter the Earth's atmosphere range from 11.2 km/s to 72.8 km/s. The entry velocity is crucial in determining if the meteoroid survives the atmosphere, mainly due to the extreme mass loss caused by the collision of the air particles with the body at high speed. For high velocities, only a massive body can generate small fragments to the

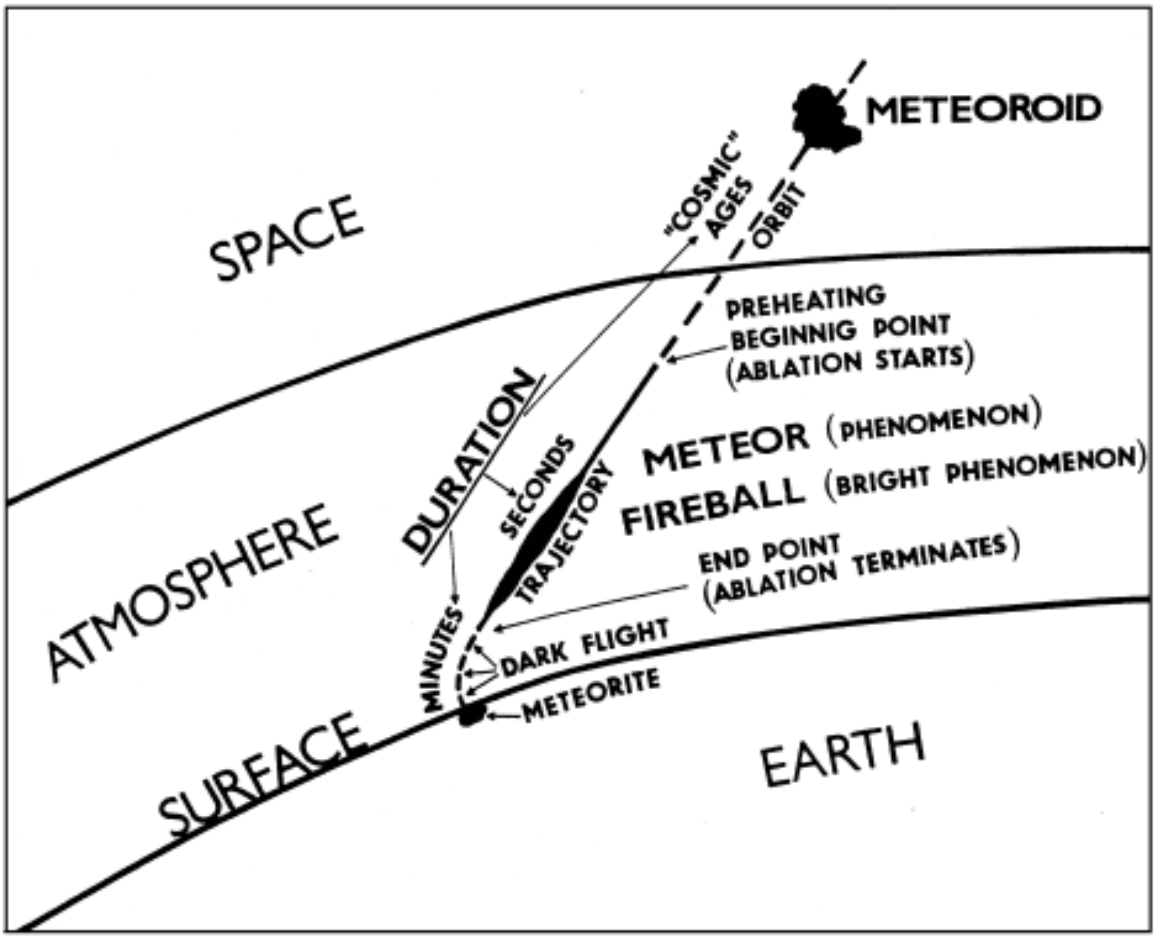

Figure 1: Meteorite fall regimes and basic terminology [6]

.

Earth's surface. For a meteoroid to impact with the ground, the velocity must not be greater than than about 30 km/s [6].

2.2 Meteor motion

The trajectory of a meteorite, from its initial orbit to the impact with the Earth surface, can be divided into five different stages:

1. **Orbital motion**

   The orbital motion is the trajectory of the meteoroid revolving around the sun, disturbed when it approaches bigger bodies. This stage usually lasts for a long time and goes from the separation from a parent body to the collision with the Earth. During this period the

trajectory can be modified by collisions, irradiation, cosmic rays and other forces.

2. **Preheating**

   The preheating starts when the meteoroid enters the atmosphere and reaches height between 300 and 100 km. The heating is mainly due to the impact of the air molecules with the body and depends on the energy transfer between them, that at the same time is proportional to v^3. This stage lasts just a few seconds and the temperature climbs up pretty fast. In fact, the temperature rises so fast that there is no time for the meteoroid to be heated all over, and it continues roughly unheated in the inside. Spallation, which means that fragments are ejected from the body, begins when the superficial tension reaches the strength of the material, which usually converges in a temperature of around 900 K for an homogeneous piece in a range from centimeters to bigger dimensions [6].

3. **Ablation**

   Ablation is the next regime of the meteoroid interaction with the atmosphere. It starts when the body starts fragmenting (when spallation begins). As the surface temperature of the meteoroid rises, the material starts melting and ultimately it evaporates from the main body and fragments. The evaporation temperature are then usually close to 2500 K. At this point, the majority of the kinetic energy is spent in the ablation, and the deceleration happens really fast, absorbing most of the kinetic energy. Only if a velocity inferior to $3km/s$ is reached at high altitudes, with a considerable mass remaining, the body keeps moving without emitting light, given that there's not enough kinetic energy to heat the surface at temperatures able to melt the material and emit light [8].

4. **Dark flight**

   The dark flight starts when the ablation stops, having decelerated the body to a velocity that is not enough to provide the kinetic energy to evaporate or heat the surface of the meteoroid. During this stage the temperature of the body quickly decreases, solidifying the surface and creating a thin crust that covers the meteorite. The crust layer is thin because the melted layer is also thin, given that during the ablation the evaporation is so fast that the is no time to conduct the heat to the interior of the body. The velocity of the meteoroid decreases to a few hundreds of m/s and the direction changes to vertical,

	Orbital motion	Preheating	Ablation	Dark flight	Impact
Time	years	seconds	seconds	minutes	instant

Table 1: Duration of the different regimes of meteor motion.

starting a free fall trajectory where the velocity decreases proportional to ρ^2. This stage usually lasts several minutes, and the wind profiles gain a transcendental importance given that the wind speed can be of the same magnitude as the meteoroid velocity and it can alter the trajectory significantly [6].

5. **Impact**

Impact velocities usually range from 10 to 100 m/s for masses between 10g to 10kg. The impact creates a little hole in the Earth's surface, somewhat bigger than the meteorite body. This hole doesn't grant any information about the motion of the meteoroid before entering the atmosphere, given that the trajectory is affected by the wind profiles in the last kilometers of the dark flight. If the ablation continues until the surface of the Earth, the crater formed is a lot bigger due to a sudden explosive release of the huge amount of kinetic energy [6].

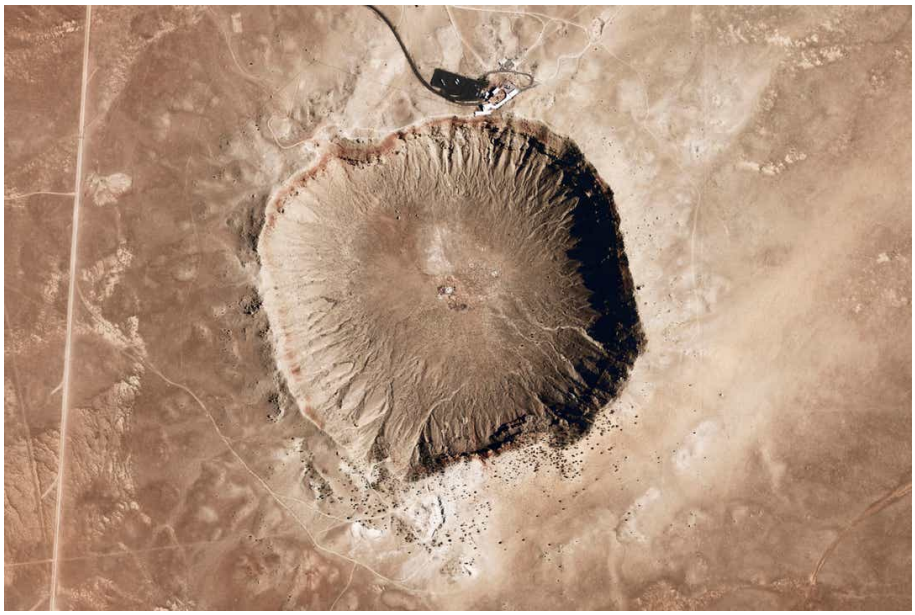

Figure 2: A meteorite impact crater in the northern Arizona desert [9].

2.3 Meteor phenomena

Depending on its initial size and velocity, meteoroids can be divided in four different phenomena:

1. **Meteoric dust**

   This phenomena is given by particles smaller than 0.01 mm and is the only one that does not emit light during the atmospheric entry. The particles are slowed down to less than a few km/s at great heights, before its temperature can rise to the evaporation point. Therefore, there is no meteor phenomena. In this case, the particle slowly falls until it reaches the Earth's atmosphere.

2. **Meteors**

   Here, we refer to the typical meteors seen by the naked eye during a meteor shower, that are produced by meteoroids larger than 0.01 mm, more or less, depending on the entry velocity. When they begin to enter the denser layers of the atmosphere, they are heated very fast until the point they start to evaporate and sublime its surface. The velocity is reduced radically during this process and ablation continues until the body looses all of its mass, which can take from a few to tens of kilometers.

3. **Meteorite falls**

   This type of meteoroid interaction happens for bodies of a size larger than 20 cm approximately. Here, the mass of the meteoroid is not completely ablated, as the meteoroid is slowed to a velocity inferior to 3 km/s before losing all the mass. The meteoroid then does not have enough energy to emit light and enters in a dark flight regime. The dark flight can last for several minutes and the velocity tends to approach to the free fall velocity of the body, which is variant with the air density [6].

   The aim of this project is to provide a method to determine where this type of meteoroids impact the surface, given that they are the most common and difficult to find type of meteorites.

4. **Explosive impacts**

This kind of phenomena is the strangest one of the mentioned. It happens when a meteoroid larger than several meters and structurally strong enough enters the atmosphere at a large velocity. For a body with such a great mass, the deceleration is small and most of the mass is not evaporated during the atmospheric flight, causing the meteoroid to impact with the Earth's surface at hypersonic velocities, creating an explosive crater much bigger than the body itself. The explosive impact can be a really dangerous phenomena, that can generate a blast wave able to damage nearby buildings and people.

	Preheating	Ablation	Dark flight	Impact
Dust	yes	no	no	no
Meteor	yes	yes	no	no
Meteorite fall	yes	yes	yes	yes
Explosive impact	yes	yes	no	yes

Table 2: Meteor regimes for the different phenomena [6].

2.4 Classification

Meteoroids can be classified by how they interact with the atmosphere, its mechanical properties or its chemical composition. The classification of meteoroids into different categories allows to define standard ranges of values of different physical properties depending on the category they are on, which can be very useful if the meteoroid has not been yet found.

Two different classifications will be exposed in this project:

2.4.1 Composition

This represents the most common way of classifying meteorites and divides them depending on its composition into three main groups:

- **Iron meteoroids**

Figure 3: Iron meteorite [10].

Iron meteoroids are mainly composed of iron and nickel metals with small amounts of sulphide and carbide minerals. The majority of them come from the core of asteroids that melt in the early history of the solar system, that, because of its high density, went to the center forming a metallic core. These meteorites are important for the understanding the formation of planetary bodies.

- **Stony-Iron meteoroids**

  Stony iron meteorites are composed of iron-nickel metal and silicate minerals in almost equal amounts, and often include semi-precious gemstones. These meteorite class is the most rare, less than 2% of the meteorites found belong to this group. Stony-iron meteorites can be classified into two main types:

  - Pallasites

    Pallasites contain big green magnesium-iron silicates crystals called olivine, which are embedded in the metal alloy. Its origin is thought to come from the border between the metal core and the olivine-rich mantle of the parent body. If this theory is correct it could reveal a lot about the Earth formation.

  - Mesosiderites

    Mesosiderites are breccias, which is a rock composed of broken fragments of

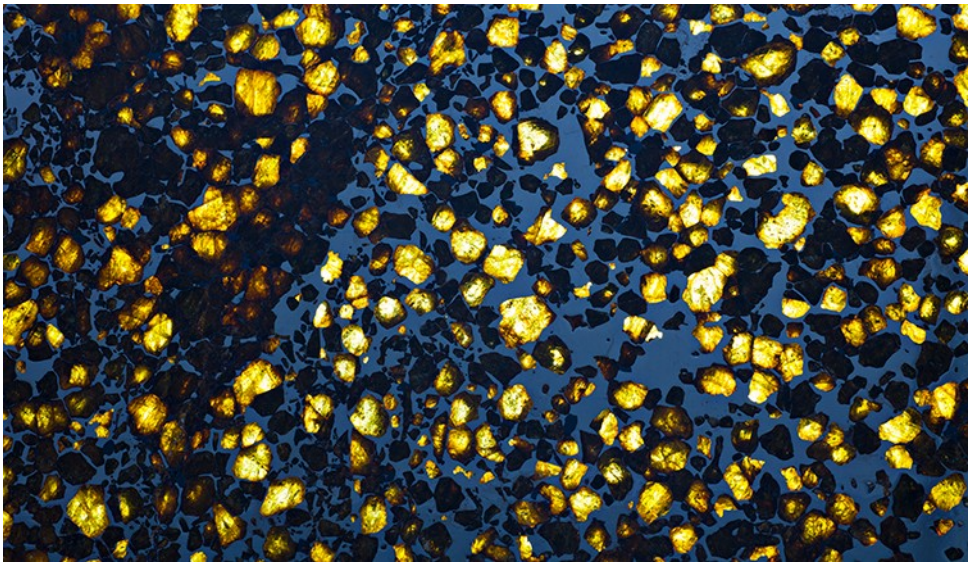

Figure 4: Meteorite of the pallasite type [10].

minerals cemented by a finer material. The fragments are made of a mix of igneous silicate and metal clasts. They are formed by the collision of two asteroids, when the rocks mix with the molten metal. They provide information of the conditions that asteroids need to melt and form iron cores.

- **Stony meteoroids**

  Stony meteorites represent the vast majority of meteorites finds and as it name indicates, they are composed mainly of minerals. There are two main groups of stony meteorites, which at the same time can be subdivided into subgroups:

  - Chondrites

    Chondrites are some of the most primitive rocks in the solar system and have never melt. They are the material from which the solar system formed.

    They are composed from droplets of silicate minerals mixed with small grains of sulphides and iron-nickel metals.

Figure 5: Meteorite of the mesosiderite type [10].

Figure 6: Stony chondritic meteorite [10].

– Achondrites

Achondrites are meteorites originating from large asteroids, Mars and the Moon. They are igneous, which means that at some point they melted into magma.

They can provide a lot of information about the structure and formation of the planets in the solar system [10, 11]

Figure 7: Stony meteorite of the achondrites type [10].

2.4.2 Ablation ability

Meteoroids can be classified by their ablation ability, including the continuous fragmentation, into four different types:

- **Group I**

  Group I meteoroids have the smallest ablation coefficients and the greatest bulk density. They are usually related to chondritic, stony meteoroids.

- **Group II**

  Group II meteoroids have a greater ablation capacity and a smaller bulk density than group I. They are usually made of fragile carbonaceous materials that mostly disintegrate in their path through the atmosphere. The Lost City, Innisfree and Príbram meteorites, which were recovered after their fall was photographed, belong to this type.

- **Group IIIA**

  Meteoroids that belong to group IIIA have a high ablation ability and a small bulk density (less than 1000 kg/m^3). They are linked to comets, as the cometary shower meteorites belong to this group.

- **Group IIIB**

  Group IIIB meteoroids are the most fragile type of meteoroids, with the highest ablation and the smallest bulk density (of hundreds of kg/m^3). Its origin is also cometary as they enter the atmosphere in cometary showers [12].

3 State of Art

The term meteor physics was invented in the last century to distinguish the observation of meteorites and its descriptive view from the study of the interaction of the meteorites with the atmosphere. The majority of processes involved in the meteor phenomena, such as the ablation and the drag force, can be well defined with simple physical principles, with only an exchange of energy and conservation of momentum being taken into account. But before having a technology that allowed sufficiently precise data of observed meteors, any physical approach was just speculative.

The recording of meteors with photographic techniques made a substantial change in the situation, as they are able not only to get precise data on the atmospheric trajectory of the meteoroid but also they allow us to convert theoretical concepts into useful tools that can explain a lot of aspects related to the meteor phenomena [13].

The first photographed and successfully recovered meteorite was the Příbram meteorite, found and recovered in 1959 [14] . Since then, efforts have been made to obtain recorded data of more meteorite falls [15].

Figure 8: Lost City flight captured on film by cameras of the Smithsonian Astrophysical Observatory's Prairie Network [16].

The next photographed and recovered meteorite was the Lost City meteorite, recovered in 1971 by the United States Prairie Network [17], followed by the Innisfree meteorite in 1977,

also in North-America, photographed by the Canadian Network [18]. Up until the 1990s, these three were the only ones found and studied to determine its pre-entry orbit and trajectory through the atmosphere.

In the last two decades the number of recovered meteorites thanks to observational recorded data has has grown considerably. So far more than 20 meteorites have been recovered thanks to photographic data. Also, a great number of cameras with the purpose of meteor observation have been installed in many countries [15].

Until the moment, very few works have been published devoted to the study of the trajectory of meteoroids in the Earth's atmosphere. They are all based on the same equations, derived from the conservation of momentum between the body of the meteoroid and the atmospheric air.

The majority of published papers, though, use these equations as a tool to obtain other data than the impact coordinates of the meteoroid. In [3], for example, they use the simulation of the trajectory for the development of a fragmentation model to calculate the energy deposition in the atmosphere. Another example is the model proposed in [4], where the trajectory equations are used as a tool to calculate the impact energy of large meteorites, regardless of the exact location of the point of impact.

But, at the end of the day, none of them are specifically focused on knowing the exact position of the meteors. Such a model is still needed, as not all the meteorites that have been recorded could be recovered, partly due to the lack of a reliable model that calculates the impact coordinates.

In this study, works focused on different aspects of the interaction of meteoroids with the atmosphere are integrated in the same code in order to obtain the most accurate impact coordinates possible.

4 Flight Mechanics

4.1 Flow regimes

A body that enters the Earth atmosphere will encounter three different flow regimes, as seen on Figure 9. This local flow regime surrounding the body will determine the heat transfer and mass loss process undergoing. The description of the flow regime is understood in terms of dimensionless parameters, and more specifically, in terms of the Knudsen number $K_n = l/R$, that represents the ratio of molecule free path l compared to a characteristic body dimension R.

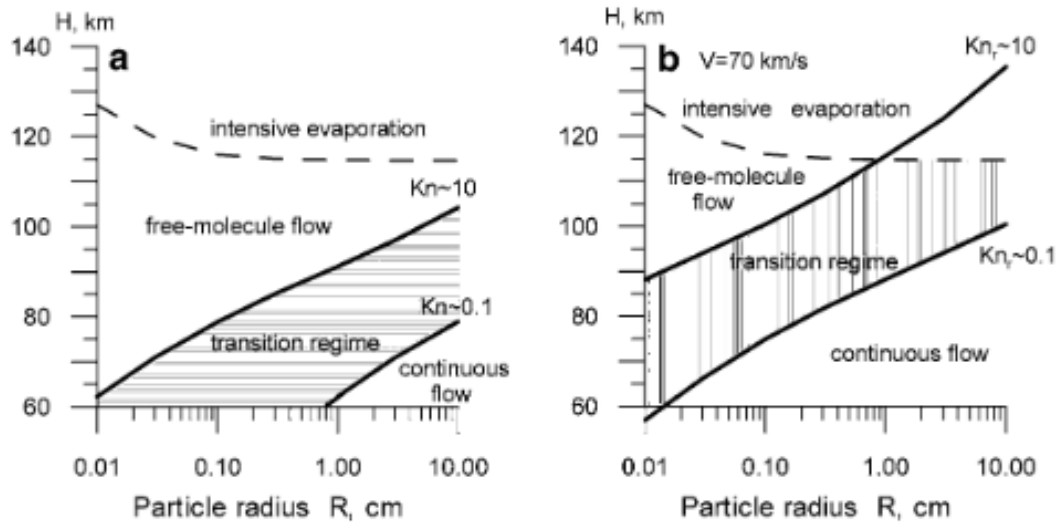

Figure 9: Boundaries of the different flow regimes for undisturbed air (a) and taking into account reflected/evaporated molecules and a velocity of 70 km/s (b) [19].

If $K_n > 10$, we find a free molecule flow, where impacts between molecules are so infrequent (low density) that is more probable for a molecule to impact again with the body than with another particle, giving all their energy to the meteoroid.

The region comprised between $K_n \approx 10$ and $K_n \approx 0.1$ corresponds to the transition flow regime, which is a flow difficult to treat analytically. As the density increases, viscous and conductive effects gain importance and a viscous layer is formed, which later will lead to a shock wave formation.

For Knudsen numbers inferior to 0.1, the flow is considered continuous, with a shockwave well formed. This flow can be well defined by hydrodynamic models. In this regime, the ablation coefficient and other important coefficients can be determined with observational data, as the body now emits light. This regime is the one assumed after the meteoroid is photographed.

4.2 Reference frames

The reference frame is the first step to describe a physical problem. The frames needed to define and develop this project are the following:

- Earth Centered Earth Fixed frame (ECEF)
- Earth Centered Inertial frame (ECI)
- Local East, North, Up frame (ENU)
- Geodetic coordinates frame
- Solar System Barycenter Ecliptic frame

4.2.1 Non-inertial frames

A non-inertial reference frame is a system that has an acceleration with respect to an inertial frame. In Newtonian mechanics, it is necessary to introduce fictitious forces (Coriolis, Centrifugal...) to the Newton's second law in order to describe the motion of bodies moving in a non-inertial frame.

Earth Centered Earth Fixed frame (ECEF)

The reference system adopted in the code for the integration of the trajectory is the ECEF coordinate system, also known as ECR or conventional terrestrial coordinate system, a frame that rotates with the Earth's rotation.

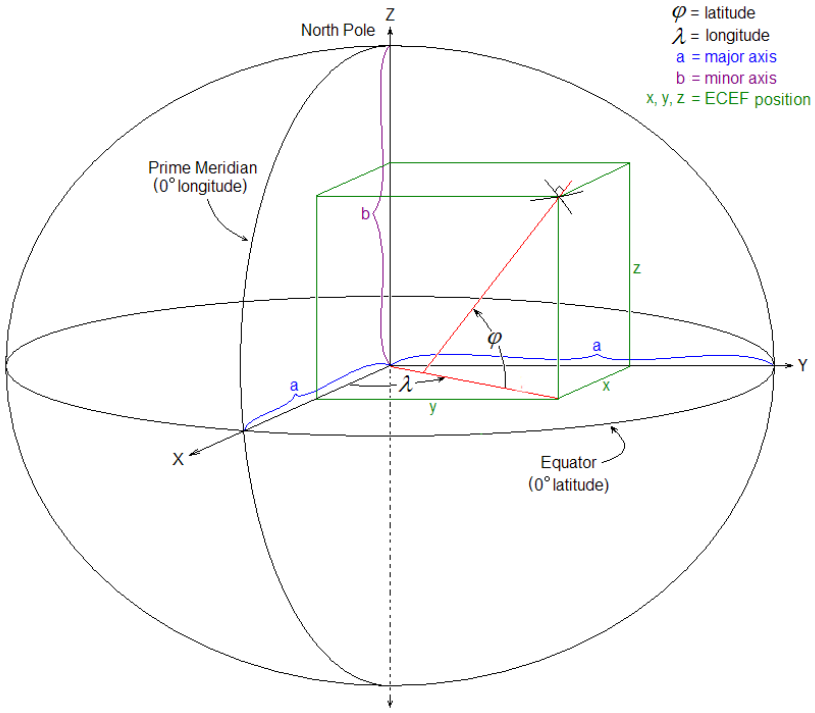

Figure 10: Earth centered Earth fixed frame and geodetic coordinates representation[20].

This coordinate system has the origin at the center of mass of the Earth.

The Z-axis points towards the North pole. The X and Y axes are contained in the plane of the equator, where the X-axis passes through the Greenwich meridian (0 degrees longitude) at the equator and the Y-axis passes at 90 degrees longitude (see Figure 10).

Geodetic coordinates frame

The geodetic reference frame is a coordinate system with origin at the center of the Earth, that approximates the Earth's surface to an ellipsoid. The locations are described in terms of longitude λ, latitude ϕ and height (see Figure 10).

The shape of the ellipsoid is defined by the World Geodetic System's latest revision WGS 84. The WGS 84 is created and maintained by the United States National Geospatial-Intelligence Agency (NGA). This model differs from the International Terrestrial Reference Frame (ITRF) by only a few centimeters[21].

Local East, North, Up frame (ENU)

The ENU reference frame defines a tangent plane to the body's position. The x and y axis are contained in this plane, with the x axis pointing towards the East, the y axis pointing towards the North and the z axis pointing up. This frame is useful to define velocities around the globe and is the coordinate system that will define the wind velocities.

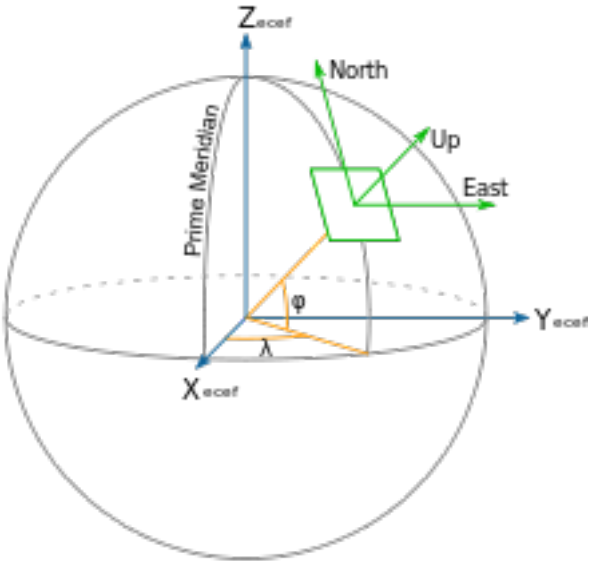

Figure 11: East, North, up frame representation [22].

4.2.2 Inertial frames

An inertial reference frame is a frame of reference that describes the time and space homogeneously, isotropically and in a time-independent manner, which means that a body without a force being applied to it does not accelerate [23].

Epoch

In order to describe an inertial reference frame it is necessary to define a reference epoch, which is the moment in time used as a reference for the coordinate system. The current most used epoch is J2000, which is in January 1, 2000 at 00:00. The prefix J indicates that it is a Julian epoch. This epoch is used to define all the inertial reference frames in this project.

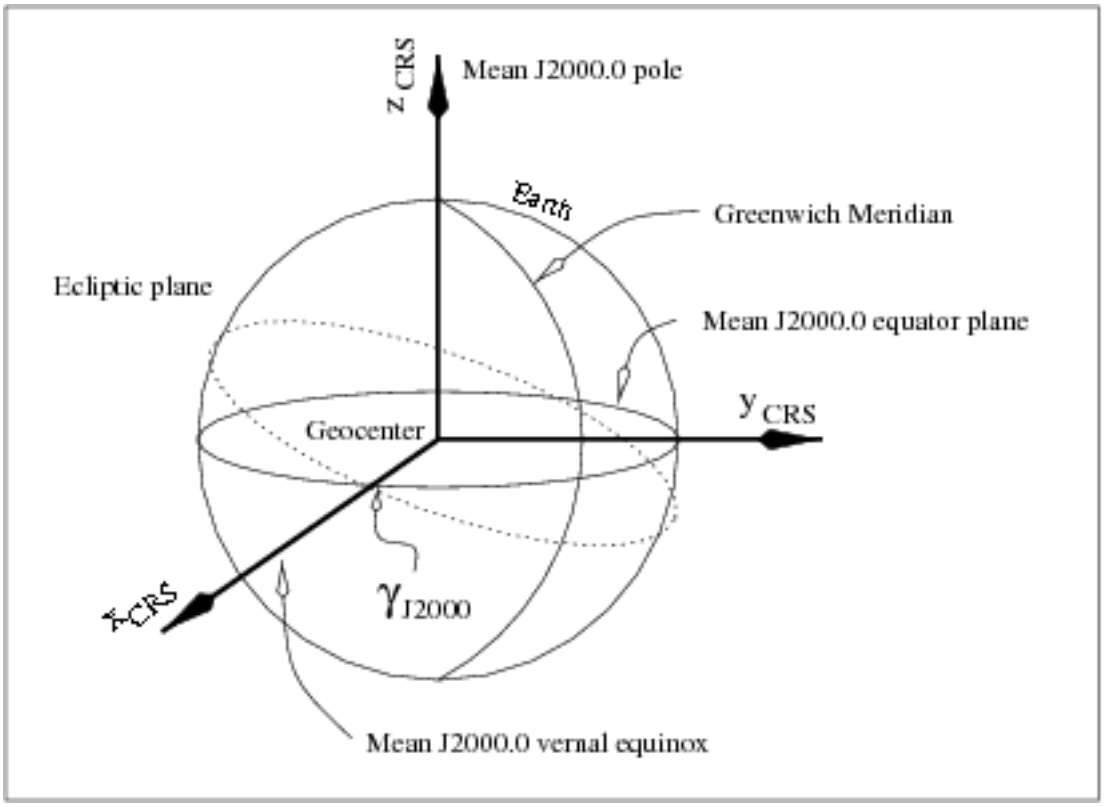

Figure 12: ECI reference frame defined by the equatorial plane [24].

Earth Centered Inertial frame (ECI)

The ECI reference frame does not rotate respect to the stars and, therefore, is not fixed to the Earth. It has the origin in the Earth's center of mass.

The ECI frame can be defined in two different planes, the equatorial plane and the ecliptic plane.

If it is defined by the equatorial plane, the x and y axes are contained in the plane of the Earth's equator, with the x axis pointing to the vernal equinox, the z axis pointing to the North pole and the y axis completes the right triangle.

If the frame is defined by the ecliptic plane, which uses the plane of the Earth's orbit, the x and y axes are contained in the ecliptic plane, with the x axis also pointing to the vernal equinox, the z axis points to the North ecliptic pole, and the y axis completes the right triangle.

The angle between Earth's equatorial and ecliptic plane is called the obliquity of the ecliptic

($\varepsilon \approx 23.4$).

Solar System Barycenter Ecliptic frame

Solar System Barycenter Ecliptic frame is a frame of reference with the origin at the solar system barycenter, as its name indicates. In order to simplify the nomenclature, this frame will be referred to as the heliocentric frame throughout this work.

The x and y axes are contained in the ecliptic plane, with the x axis pointing towards the vernal equinox, the z axis pointing to the North ecliptic pole, and the y axis completing the right triangle, just the same as the ECI reference frame, only with the difference in the origin.

4.3 Frame transformation

Geodetic coordinates to ECEF position

The conversion from geodetic coordinates (longitude, latitude, altitude) to ECEF and vice-versa is done with a Matlab function called lla2ecef, from the Aerospace Toolbox[25].

ECEF to ECI (equatorial)

The conversion from ECEF to ECI in the equatorial plane is also carried out thanks to the functionalities of the Matlab Aerospace Toolbox. The function being used is called ecef2eci, and it is able to transform positions, velocities and accelerations from ECEF to ECI coordinates.

ECI (equatorial) to ECI (ecliptic)

The conversion of ECI coordinates and velocities from the equatorial plane to the ecliptic plane consists of a simple frame rotation in the x axis of $\varepsilon \approx 23.4$. The rotation matrix is exposed below:

$$R_x(\varepsilon) = \begin{pmatrix} 1 & 0 & 0 \\ 0 & \cos\varepsilon & -\sin\varepsilon \\ 0 & \sin\varepsilon & \cos\varepsilon \end{pmatrix} \tag{1}$$

ECI (ecliptic) to Solar System Barycenter Ecliptic

The conversion from the ECI to the Solar System Barycenter Ecliptic consists in adding the position of the Earth in heliocentric coordinates to the position in ECI, so that the center of coordinates is moved to the Solar System Barycenter.

$$\vec{y}_h = \vec{y}_{ECI} + \vec{y}_{earth_h} \tag{2}$$

The position of the earth in heliocentric coordinates is obtained using SPICE, an ancillary information system that provides scientists and engineers the capability to include space geometry and event data into mission design, science observation planning, and science data analysis software [26].

4.4 Inertial forces

Newton's laws are only valid if applied to an inertial reference system. However, it is possible to apply classical mechanics to a non-inertial reference system introducing fictitious forces. An inertial force, also called fictitious force, is a force that appears when describing the movement of a body with respect to a non-inertial reference system in order to correct Newton's second law ($\sum F = ma$).

Given that the main reference frame used in the integration of the meteoroid trajectory is a non-inertial one (ECEF), it is necessary to introduce these forces before introducing the real forces.

The acceleration of a particle in a fixed reference system a_P and in a moving reference system a_M which rotates with an angular velocity Ω respect to the fixed reference system, are related by the following expression:

$$a_F = a_0 + \dot{\Omega} \times r + \Omega \times (\Omega \times r) + 2\Omega \times \dot{r} + a_M \tag{3}$$

where a_0 is the acceleration of the origin of the moving reference system, $\dot{\Omega} \times r$ is the tangential acceleration, $\Omega \times (\Omega \times r)$ is the centrifugal acceleration and $2\Omega \times \dot{r}$ is the Coriolis acceleration [27].

In order to describe the motion of a particle in a non-inertial reference system, it is necessary to know the expression of ma_M.

The Newton's second law defines that the equation of motion in an inertial reference system is given by:

$$\sum F = ma_F \tag{4}$$

where F are the forces acting on the particle. Then, substituting equation 3 in equation 4, the equation of motion in a non-inertial reference system is given by:

$$\sum F - ma_0 - m\dot{\Omega} \times r - m\Omega \times (\Omega \times r) - 2m\Omega \times \dot{r} = ma_M \tag{5}$$

In this study, the main integration is carried out in the Earth Centered Earth Fixed reference frame, where the angular velocity corresponds to the Earth's rotational velocity, and the terms $\dot{\Omega}$ and a_0 are null. The resulting equation of the acceleration is the following:

$$\sum F/m - \Omega_E \times (\Omega_E \times r) - 2\Omega_E \times = a_M \tag{6}$$

where F/m represents the acceleration of the physical forces that act on the meteoroid, which are explained below.

4.5 Real Forces

During a meteoroid's path through the atmosphere, there are two main forces acting upon it:

- Gravitational Force
- Drag Force

4.5.1 Gravitational Force

The gravitational force is defined by the Newton's law of universal gravitation, which states that every particle attracts every other particle in the universe with a force which is directly proportional to the product of their masses and inversely proportional to the square of the distance between their centers and with a direction pointing the center [28].

$$F_g = G\frac{m_1 m_2}{r^2} \tag{7}$$

Here, F is the gravitational force acting between two objects, m1 and m2 are the masses of the objects, r is the distance between the centers of their masses, and G is the gravitational constant.

To find the acceleration caused by the Earth to the meteorite, the force is divided by the mass of the meteor:

$$\vec{a} = -G\frac{M_T}{r^2}\frac{\vec{r}}{|r|} \tag{8}$$

the direction is given by the unitary vector $-\frac{\vec{r}}{|r|}$ which points to the Earth's center of gravity.

4.5.2 Drag Force

The drag force can be modeled by taking into account the conservation of momentum between the meteoroid and the atmospheric air, which is based on simple physics. This model has been assumed in multiple related articles given that the equations are pretty simple and at the same time they give a good approximation of the drag force [6, 12, 13, 19, 29, 30].

In the case of a meteoroid, with mass (m), density (ρ_m) and cross-sectional area (S), entering the Earth's atmosphere at a velocity (v) and having a drag coefficient (C_D). The cross-sectional

area of the meteoroid can be defined through:

$$S = A_s(\frac{m}{\rho_m})^{2/3} \tag{9}$$

where A_s represents a dimensionless shape factor which relates the cross-sectional area of the meteor to its volume (V_m): $A_s = \frac{S}{V_m^{2/3}}$

The value of A_s depend on the shape of the meteoroid. Because of the difficulty of extracting reliable data of a meteoroid's shape and size, this parameter is used instead, as it is close to a unity for most shapes. Since the meteoroids usually rotate during their flight through the atmosphere, it is generally assumed that irregularly shaped bodies will have their shape factor approach of a sphere [31].

Now, when the meteoroid passes through the atmosphere, it sweeps a volume of air of size $Svdt$ in a time dt. The mass of this volume (m_a) can be calculated with the atmospheric density (ρ_a) as $dm_a = \rho_a Svdt$.

If S is substituted from Equation 9, the expression for the rate of change of air mass by unit time is obtained [29]:

$$dm_a = \rho_a A_s(\frac{m}{\rho_m})^{2/3}vdt \tag{10}$$

Due to the impact of air molecules with the meteoroid, this air volume will transfer momentum to the meteoroid, which result in a change of momentum of the meteoroid:

$$\frac{d(mv)}{dt} = v\frac{dm}{dt} + m\frac{dv}{dt} \tag{11}$$

At the same time, the air particles in this volume will gain momentum per unit time:

$$\frac{C_D}{2}\frac{dm_a}{dt}v = \frac{C_D}{2}\rho_a A_s(\frac{m}{\rho_m})^{2/3}v^2 \tag{12}$$

The drag force is defined as a force acting in the opposite motion of an object moving inside a fluid. The drag equation can be derived through conservation of momentum by simply

equating the loss of momentum per second of the meteoroid with the momentum gained per second by the volume of air:

$$\frac{dv}{dt} = -\frac{C_D A_s \rho_a v^2}{2\rho_m^{2/3} m^{1/3}} \tag{13}$$

The negative sign is added to indicate the deceleration of the meteoroid [31].

The drag equation is usually modified adding a coefficient called shape-density coefficient, which can be estimated with observational data [3, 13].

$$K = \frac{C_D}{2} A_s \rho_m^{-2/3} \tag{14}$$

The resulting drag equation is the following:

$$\frac{d\vec{v}}{dt} = -K\rho_a m^{-1/3} v^2 \frac{\vec{v}}{|v|} \tag{15}$$

where the only unknown parameter for the integration is the shape-density coefficient, which can be taken as an average along the trajectory or varying along it. The direction of the acceleration due to the drag force is contrary to the velocity and is given by $-\frac{\vec{v}}{|v|}$ [19].

The mass in this equation, as well as all the equations included in this project, is based on the deceleration of the largest, brightest fragment and is called the dynamic mass, which can differ significantly from the photometric mass, which takes into account the ablation of small fragments too.

4.6 Ablation

The term of meteoroid ablation refers to the mass leaving the surface of the body either by vaporization, as liquid droplets. In this work the ablation takes into account the continuous fragmentation too, which is the constant fragmentation into small fragments. On the other hand, the sudden or gross fragmentation is treated as a different phenomena, and it is described in section 4.9

The ablation phenomena can be well described through an energy balance between the air and the body. This methodology has been widely used for the calculation of meteoroid entry dynamics, and it has been proved to give a good approximation of the mass loss due to ablation [6, 12, 13, 19, 29, 30].

The standard heat balance equation per unit of surface for a spherical body, assuming an isotropic energy flux can be written as:

$$\frac{1}{2}\Lambda\rho_a v^3 = 4\varepsilon\sigma({T_s}^4 - {T_0}^4) - \frac{Q}{A}\frac{dm}{dt} + \frac{4}{3}R\rho_m c\frac{dT_{av}}{dt} \tag{16}$$

where R is the meteoroid radius, A is the cross-sectional area, Λ is the heat transfer coefficient, Q is the specific ablation energy (energy necessary for the ablation of a unit mass), c is the specific heat, ρ_a and ρ_m are the atmospheric and meteoroid densities,ε is the emissivity, σ the Stefan-Boltzmann constant,T_s, T_{av}, T_0 are the surface temperature of the meteoroid, some uniform body temperature and the ambient temperature [19].

Theoretically, Equation 16 means that the energy coming from the incoming air molecules (left side) is converted into thermal radiation cooling (first term of the right side), ablation (second term), and heat conduction (third term).

The altitude at which the energy received from the air molecules becomes greater than the energy lost on thermal radiation cooling and heat conduction may be called height of intensive evaporation, following the nomenclature in [19], and is comprised between 110-130 km for porous bodies. Below this height, the incoming energy is spent almost exclusively in the ablation, and heat conduction and thermal radiation cooling may be neglected from the heat balance [6, 8].

Taking into account this consideration, the mass loss equation then can be written as:

$$\frac{dm}{dt} = -\frac{1}{2}\frac{A\Lambda\rho_a v^3}{Q} \tag{17}$$

The mass loss equation, like the drag equation, is also commonly modified so that it is function to coefficients that can be determined with observational methods. These coefficients are the shape-density coefficient (Equation 14) and the ablation coefficient:

$$\sigma = \frac{\Lambda}{QC_D} \tag{18}$$

The resulting mass-loss equation is the following:

$$\frac{dm}{dt} = -K\rho_a \sigma m^{2/3} v^3 \tag{19}$$

where the unknown parameters for the integration are the two coefficients mentioned above, which can too remain constant or vary along the trajectory.

4.7 Atmosphere Model

The atmospheric density is the mass per unit volume of Earth's atmosphere. It is a crucial parameter for the calculation of the trajectory of a meteoroid, given that both the ablation and the drag force depend deeply of it (See Equations 13 and 19). Hence, it is really important to choose an adequate atmospheric model.

Three different atmospheric models are compared for this project:

- **U.S. Standard Atmosphere, 1976**

  This atmospheric model represents an idealized, steady-state representation of the earth's atmosphere from the surface to 1000 km, which means that seasonal, latitudinal, and solar cycle associated variations of atmospheric parameters are not taken into account, and a period of moderate solar activity is assumed. All this data is defined by a series of functions and observational data of various kinds and has been tabulated by the NASA [32].

  This model is available in the Aerospace Toolbox of MATLAB. Above 84,852 m, temperature values are extrapolated linearly and pressure values are extrapolated using a logarithmic function. Density and speed of sound above this altitudes are calculated using a perfect gas relationship [33].

- **International Standard Atmopshere (ISA)**

The International Standard Atmopshere, similar to the U.S. Standard Atmosphere, is also a static atmospheric model, meaning that the physical properties of the atmosphere change as a function of the altitude. This model was created by ICAO and it is mainly used for civil aviation. It provides accurate data until 86 km of height.

A Matlab implementation of this model is also available in the Aerospace Toolbox. This implementation assumes that temperature and pressure values are held constant for altitudes above 20 km [34].

- **NRLMSISE-00**

  The NRLMSISE-00 model is an empirical model developed by the U.S. Naval Research Laboratory and published in 2001. This model calculates the temperature and air density from ground to space around the globe, and it is also able to predict the amount anomalous oxygen. This model is the current standard atmospheric model for international space research, and is widely used for low Earth orbit satellites.

  In contrast to the U.S. Standard Atmosphere and the ISA, this model takes into account the seasonal, latitudinal, and solar cycle associated variations of atmospheric parameters [35].

  This model is also available in the Aerospace Toolbox of MATLAB and the data of solar activity is retrieved from the NOAA database automatically [36].

Comparison between models

In order to choose the mot suitable model, temperature and density are compared for heights until 120 km, which is the maximum height where the meteorite usually begins to light up.

Figure 13 shows that both the U.S. Standard Atmosphere and the NRLMSISE-00 return very similar density values. The ISA model, on the other hand, approximates the values well up to a height of 20 km and then keeps them constant.

Unlike density, temperature values differ more among all models. The model that best approximates the temperature is NRLMSISE-00, since the ISA model leaves the values

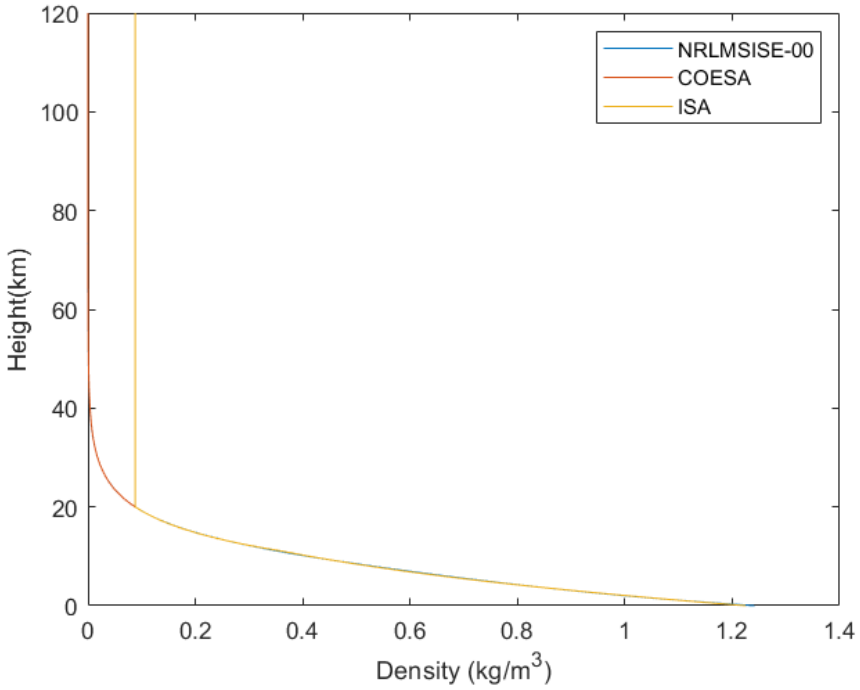

Figure 13: Density from 0 to 120 km.

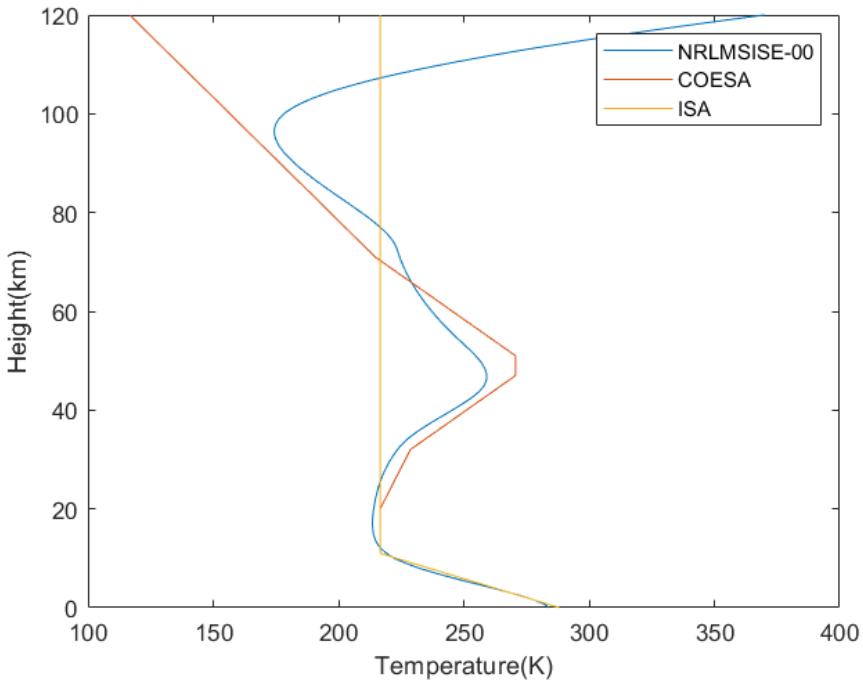

Figure 14: Temperature from 0 to 120 km.

constant from 20 km height and the COESA model makes the temperatures from 84 km height decrease linearly, which is not realistic.

Overall, the model that best approximates the physical properties relevant for the problem for thwe heights that are required is the NRLMSISE-00, while at the same time, it does not does not represent a much higher computational cost than the other models. Therefore, the NRLMSISE-00 is the model adopted in the project.

4.8 Wind Model

The atmospheric wind model is provided by the NOAA's (National Oceanic and Atmospheric Administration) Global Forecast System (GFS), a weather forecast model that covers the entire globe with a base horizontal resolution of 28 kilometers between grid point. The GFS is a coupled model, composed of an atmosphere model, an ocean model, a land/soil model and a sea ice model, which work together to provide with accurate data of the weather conditions. The gridded data is obtained through the NOAA National Operational Model Archive and Distribution System (NOMADS), which returns data of the wind conditions around the globe every 6 hours [37].

The gridded data gives the velocity in the directions east, north and up (ENU) every 0.5 degree of latitude and longitude and for altitudes up until 30 km. Even though this wind model does not cover the entire trajectory, the wind does not become important until the density begins to be a significant parameter and the velocities of the wind are of the same magnitude of the meteoroid velocity, which usually happens near altitudes of 30 km. For this reason, the assumption that the wind starts at a height of 30 km is considered valid.

In Figure 15 the velocity of the meteoroid is plotted as a function of the height. In this case the velocity of the fragments goes under hundred meters per second (the wind velocity rarely surpass this value) at a height of 25 km approximately. At the same time, Figure 3 shows that the density does not begin to grow significantly until about 30 km.

To obtain the wind speeds, two different interpolation methods have been tested. In the first one, the speeds were interpolated for each instant of time of the integration while in the second one, the coordinates were set at the average point of ground impact and interpolated

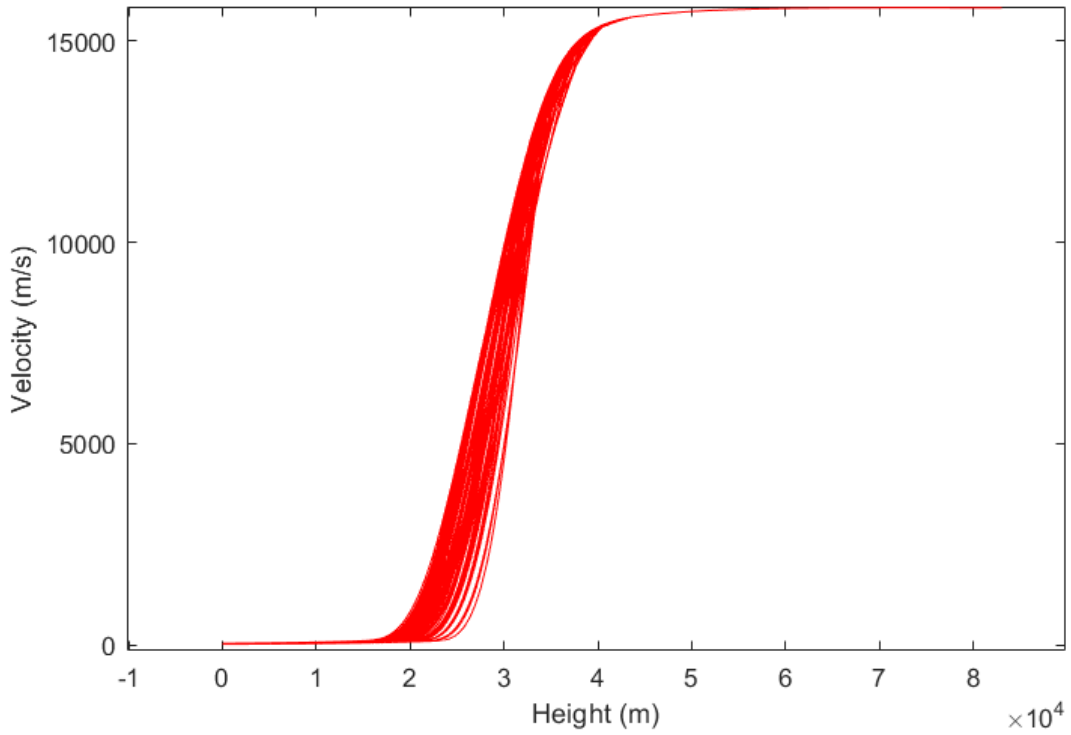

Figure 15: Velocity as a function of the height for all the fragments of one simulation.

as a function of the height.

After performing a simulation with each method, it is decided to use the second one for to reasons. Firstly, the simulation time if interpolated with the first method is more than 100% slower than with the second one. Secondly, the wind velocities at the starting point of the trajectory are the same that the ones at the end of the trajectory because of the poor precision of the wind model (points every 28 km) and therefore, this wind model can only give a qualitative measurement of the wind.

The position and time of the wind velocities are interpolated linearly as a first approximation, although a sensibility analysis of the wind is later carried out in order to check the importance of choosing this interpolation model, given that the wind velocities can change in a significant way in 6 hours.

4.9 Fragmentation

Fragmentation is one of the most important points modelling the trajectory of a meteoroid entering the Earth's atmosphere. It is also one of the most complicated one, as there is no way to predict the number of child fragments or its velocity and mass that result of each fragmentation. There are many factors, such as the shape of the meteoroid, its composition, or weak points or cracks, that cannot be calculated or predicted that make it difficult to study.

As seen on section 2, there are two major fragmentation phenomena:

- Continuous fragmentation: where the meteoroid is treated as a single fragmenting body and and is defined by the mass loss equation (Equation 19).
- Sudden fragmentation: which represents a major fragmentation event, where the main body loses a significant part of the mass at a certain instant of time. It is also referred as gross or discrete fragmentation.

The fragmentation model in this work refers only to the sudden fragmentation events, given that the continuous fragmentation is already defined by the ablation of the meteoroid.

Previous models

The majority of existing fragmentation models consider either a liquid drop model or a discrete fragmentation model.

In the liquid drop models, also referred to as pancake models, the meteoroid is treated as a single deforming body, that begins to deform and expand into a "pancake" shape when the breakup point is reached (Figure 16). This deformation increases the cross-sectional area of the meteoroid, which at the same time increases both the drag force and the mass loss of the bolide. These approaches have been widely used to model the luminosity and the energy dissipated in the atmosphere by asteroids, although they are not really useful for trajectory calculations [3, 38].

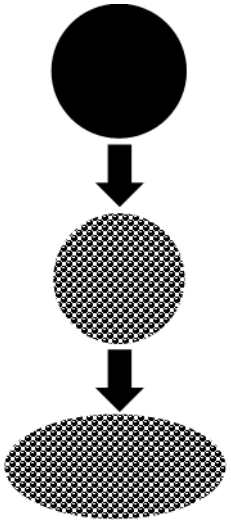

Figure 16: Schematic liquid drop model.

The discrete models, in contrast, consider successive breakup events that convert the body in smaller fragments (Figure 17). In each breakup the meteoroid is fragmented in smaller individual pieces, that at the same time are treated as a single body. These approaches have been used to calculate both energy deposition in the atmosphere and trajectories of meteoroids and they usually consider stochastic parameters, such as α, σ and the fragmented masses, for the calculations [4, 39].

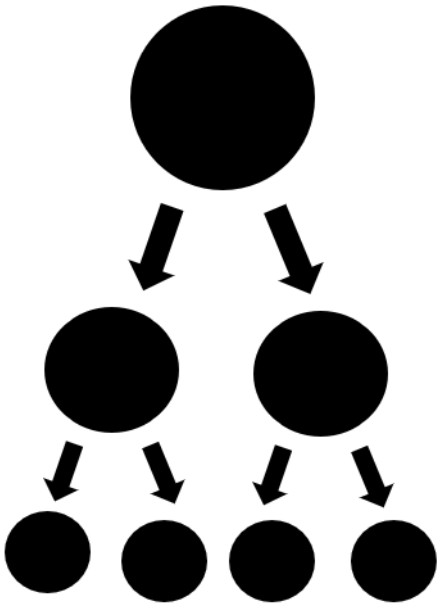

Figure 17: Schematic discrete fragmentation model.

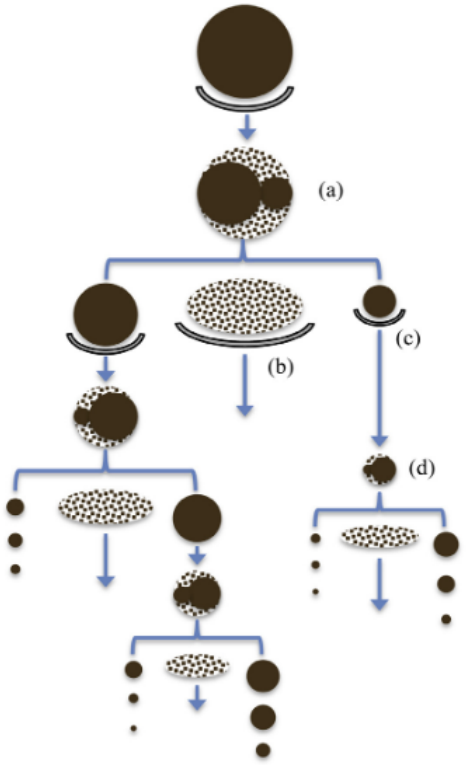

Figure 18: Schematic hybrid fragmentation model [3].

Finally, some hybrid models have also been presented, combining both the discrete and the liquid drop models, the most extensive hybrid model is presented in [40]. In each fragmentation the meteoroid is divided into a number of discrete pieces plus a debris cloud. Then the discrete pieces are then integrated individually and the debris cloud is also integrated, but following a liquid drop modelling. This model has been show very useful to calculate the energy deposition of meteoroids [3].

4.9.1 Fragmentation model

The fragmentation model adopted in this project is an hybrid model, where, in each fragmentation event, the meteoroid splits into a number of fragments and a percentage of debris cloud. After each fragmentation event, the trajectories of the child fragments are integrated individually, while the debris cloud is considered to be disintegrated before impacting with the ground and therefore is not integrated.

4.9.2 Breakup criteria

A sudden fragmentation is assumed to occur when the dynamic pressure at the leading edge stagnation point exceeds a specified threshold, σ, as seen on Equation 20 [4, 41].

This parameter has been widely referred to as "strength", but it does not represent a specific property of the material, such as the compressive strength or the tensile strength. What this parameter really represents is the strength of the aggregate that conforms the meteoroid and defines the flight conditions under which the breakup begins to manifest observably. This value depends on the internal fracture and existing fracture patterns of the meteoroid, given that in general, the body is not homogeneous. This value of the threshold is usually smaller than the material strength.

$$\rho_a v^2 \geq \sigma \tag{20}$$

The strength of the resulting fragments increases every time a breakup occurs. That is because the crack size scales with the size of the body, so that larger bodies have larger cracks [3].

The breakup strength of the child fragments increase following a Weibull distribution, as exposed on Equation 21.

$$\sigma_c = \sigma_p (\frac{m_p}{m_c})^{\alpha} \tag{21}$$

where α is an exponential strength scaling parameter, and the subscripts c and p refer to the child and parent fragments [4, 3].

4.9.3 Fragmentation event

Masses

In each fragmentation event, the parent body is split into two child fragment and a mass of dust.

The first fragment occupies 50 to 99 % of the mass of the parent fragment randomly, while the rest is divided between the second fragment and the dust mass, also referred to as 'cloud' mass, which is not considered for the integration as the individual masses of the dust fragments are considered too small to be recovered.

Velocities

The aerodynamic interaction between separating bodies in supersonic speed flow was first studied in 1980 by Passey & Melosh [42]. In their study they focused on the separation of two spherical bodies assuming only lateral separation the bodies. Following their nomenclature the larger fragment will be referred to as primary body and the other fragments as secondary bodies.

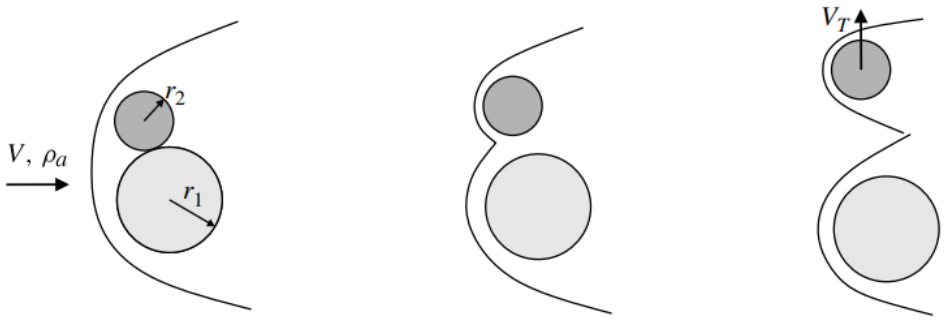

Figure 19: Separation model proposed by Passey & Melosh [42].

They proposed a scaling law for the lateral velocity of the smaller body, that is directly related to the relation of radius $\frac{r_1}{r_2}$, the ratio between the atmospheric and the meteor densities $\frac{\rho_a}{\rho_m}$, and the velocity of the flow:

$$V_T = \sqrt{C \frac{r_1}{r_2} \frac{\rho_a}{\rho_m}} V \tag{22}$$

Here , C is a constant that lies between the values of 0.03 and 2.25 and that was first determined through the examination of multiple crater fields.

In 2011, Laurence & Deiterding showed that the model proposed by Passey & Melosh did not predict satisfactorily the separation behavior of two bodies with different sizes. That is

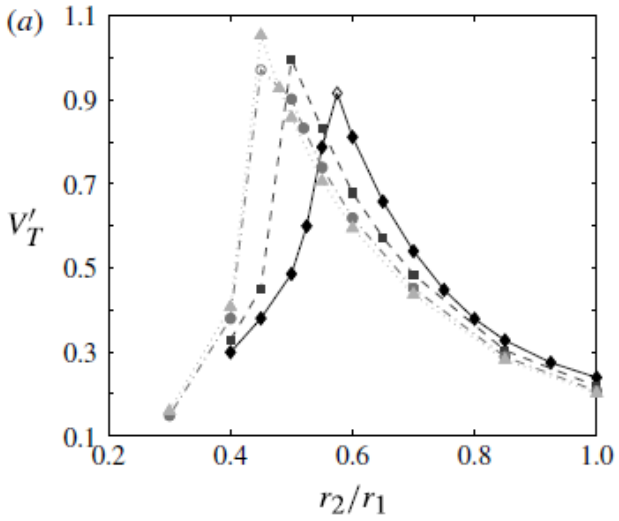

Figure 20: Normalized separation velocity as a function of the ratio of the fragments size. diamond, Ma = 4; square, Ma = 6; circle, Ma = 10; triangle, Ma = 25 [44].

because the smaller body perceives a higher axial acceleration and then travels both laterally and downstream relative to the larger body [43].

They conducted an experimental and computational investigation of the unsteady separation behaviour of two spheres. With the data resulting from the study they computed the normalized separation velocity of the smaller body as a function of the ratio of the size of the fragments for different Mach numbers. The normalized velocity is used to calculate the constant C as it follows:

$$C = V'_T \frac{r_2}{r_1} \tag{23}$$

this constant is then used to compute the Lateral velocity of the smaller body [4, 44].

As we can see on Figure 20, for all the Mach numbers there is a peak in the separation velocity between ratios from 0.4 to 0.6. This phenomenon is referred to as 'shock wave surfing', as the smaller body follows the trajectory of the bow shock of the primary body downstream (As seen on Figure 21c), gaining a significantly larger lateral velocity that would be impossible otherwise. Bodies with smaller radius than the critical (Figure 21a) do not develop a sufficient lateral velocity in the early stages of separation and quickly enter the flow region inside the main body bow shock. Bodies with larger radius than the critical (Figure 21e), are quickly

kicked out of the bow shock and thus the lateral velocity is also smaller.

Following this approach, the velocities of the secondary bodies are computed with the scaling law of Passey & Melosh and taking the values of the normalized velocities proposed by Laurence & Deiterding. The direction of the lateral velocity has to be perpendicular to the direction of the parent fragment velocity, so it that it has two degrees of freedom in that plane. The direction respect to the perpendicular plane is computed randomly. If the secondary body has a ratio that is smaller than the data available in Figure 20, the lateral velocity is assumed to be null, and it remains attached to the bow shock.

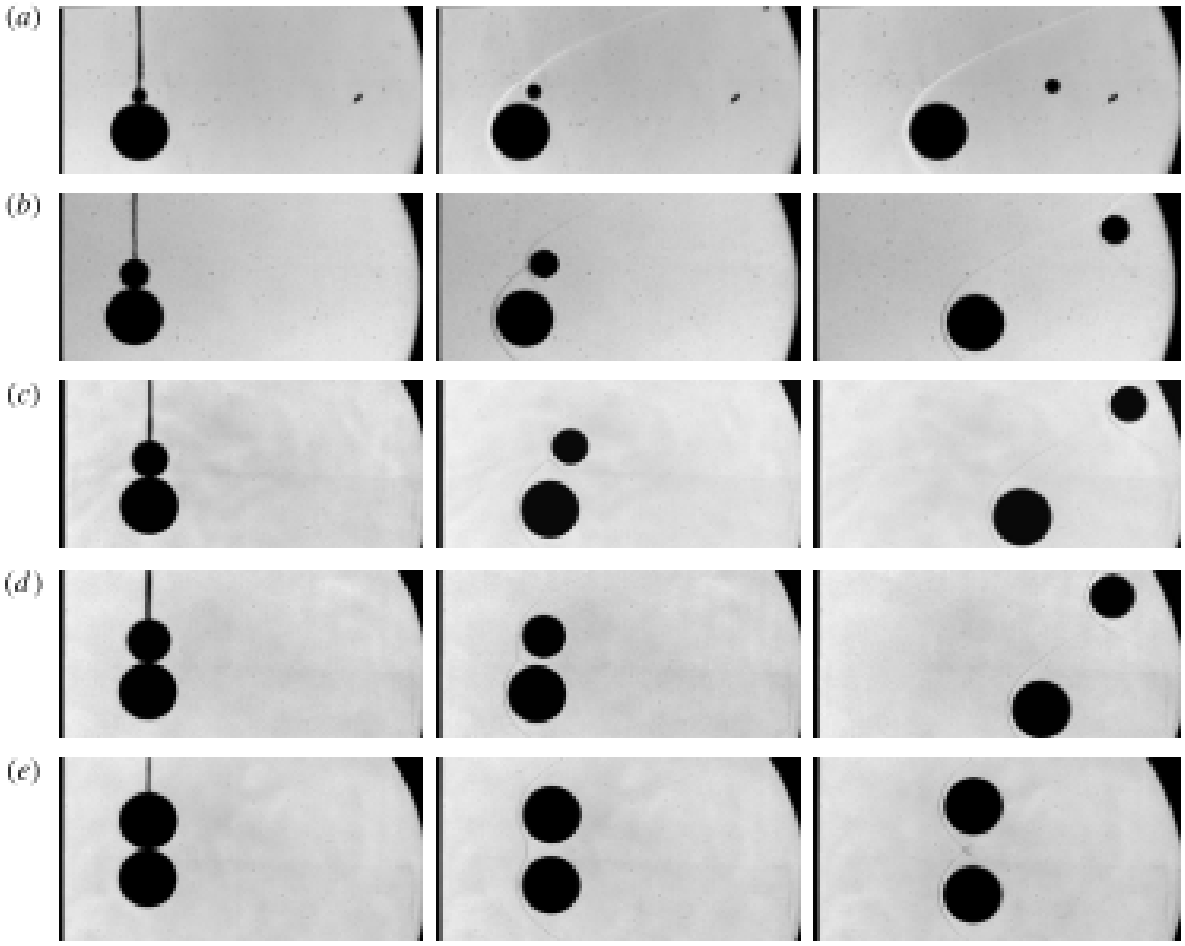

Figure 21: Separation behaviour for configurations with various radius ratios and (approximate) initial alignment of the sphere centres in the axial direction [44].

Finally, the velocity of the primary body is calculated through the conservation of moment between all the fragments, which usually results in a very small lateral velocity for the larger

body:

$$m_1\vec{V}_1 + \sum_{i=2}^{nf} m_i\vec{V}_i = m_p\vec{V}_p \tag{24}$$

where the subscript 1 correspond to the primary fragment (larger fragment), the subscript i to the secondary fragments and the subscript p to the original parent fragment before the fragmentation event.

5 Orbital mechanics

In this section the orbital motion of the meteoroid around the Sun will be studied. As a starting point, in order to define the motion of the meteoroid, Newton's *Universal Law of Gravitation* is introduced. For a two-body system with masses m_1 and m_2, the forces that exercise one body over the other are defined by:

$$\vec{F_1} = G\frac{m_1 m_2}{r^3}\vec{r} \qquad \vec{F_2} = G\frac{m_1 m_2}{r^3}\vec{r} \tag{25}$$

where $\vec{r}$ is the unitary vector pointing from the center of gravity of the body 1 to the center of the body 2, and G the universal gravitational constant.

In order to simplify the problem, the following hypothesis are taken into account:

1. The orbit of the meteoroid intersects the orbit of the Earth, meaning that the Earth's gravity does not have a significant effect. This hypothesis is followed in the majority of related articles and therefore it is also applied in this project [6, 30, 45, 15, 46].

2. The system formed by the sun and the meteoroid is isolated from the rest of the universe, meaning that only the force of mutual attraction between the two bodies is considered (Two body problem).

3. The masses can be considered punctual and localised in the centre of gravity of each of the body [47].

Taking into account the above hypothesis, the integration of the dynamic equations is used to obtain the relative movement between the meteoroid and the sun.

Centering the origin of coordinates in the Solar System barycenter, the relative motion of the meteoroid around the sun corresponds to a conic and is defined by the equation, that describes the motion orbit's plane (2D):

$$r = \frac{h^2}{\mu}\frac{1}{1 + e\cos\theta} \tag{26}$$

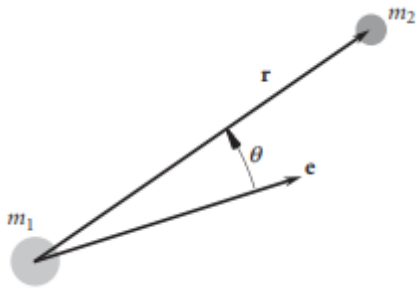

Figure 22: Parameters of the orbit equation illustrated [48].

where r is the radius of the position of the meteoroid, h is the modulus of the relative angular momentum of the meteoroid, θ is the true anomaly, e is the eccentricity (the magnitude of the eccentricity vector, pointing to the periapsis of the orbit) and μ the gravitational constant of the sun (GM_sun). These variables are clearly illustrated in Figure 22.

5.1 Orbital elements

The classical orbital elements are the six Keplerian elements, which allow to determine the position and velocity of a body orbiting another body for any instant of time.

Before defining the orbital elements its is necessary to introduce some concepts. First of all, the plane of reference is the plane of the Earth's orbit and the orbital plane is the one in which the meteoroid is moving. Secondly, the node line is the intersection of the orbital plane with the reference plane. Finally, the points in which the orbit intersects the node line are called ascending and descending node, depending on the direction of the meteoroid at that point (see Figure 23.

Having introduced these concepts, the orbital elements can be defined as:

- Semi-major axis (a): semi-major axis of the ellipse of the orbit, which corresponds to the sum of the perigee and apogee distances divided by two.
- Eccentricity (e): shape of the ellipse, it defines how elongated the ellipse is.
- Right ascension of the ascending node (Ω): angle between the x-axis and the ascending node

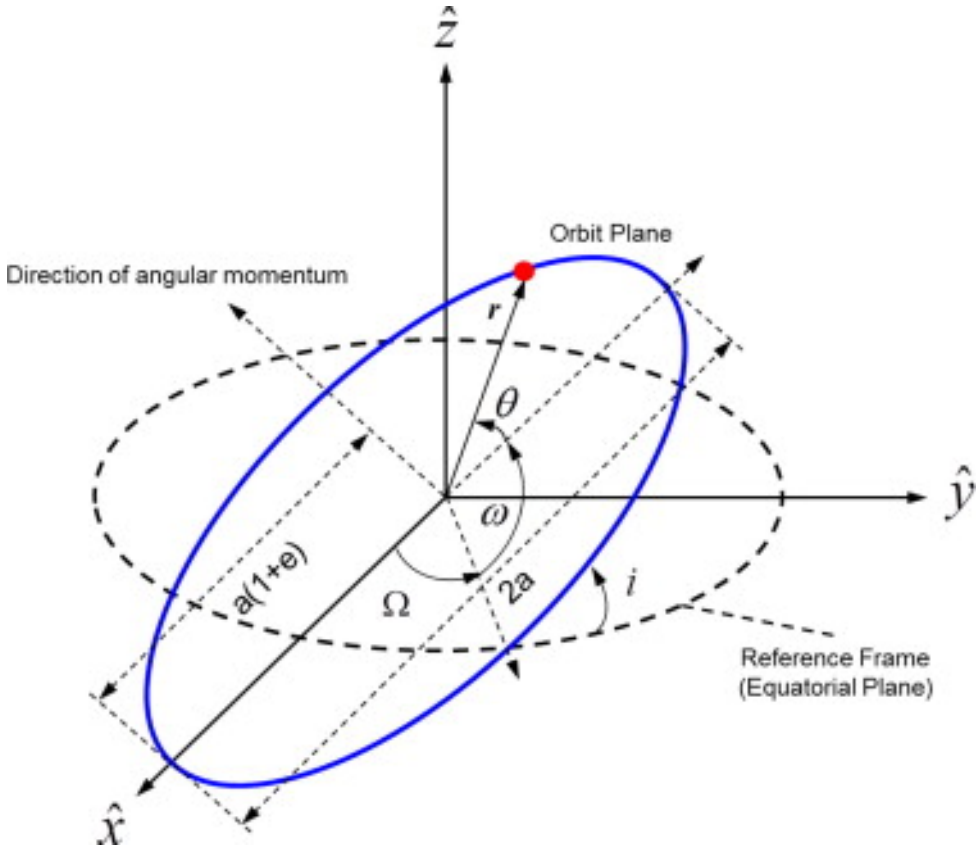

Figure 23: Orbital elements associated with an inertial reference frame [49].

- Inclination (i): angle between the plane of reference and the orbital plane.
- Argument of perigee (ω): angle between the node line vector and the eccentricity vector, measured in the plane of the orbit.
- True anomaly (θ): angle between the perigee and the position of the body movement-wise, measured in the plane of the orbit.

5.2 Heliocentric state vector

To determine the orbital elements of a body, it is sufficient with the velocity and the position of the body at a certain instant of time (state vector). In the case of the determination of a meteoroid's orbit, the state vector should be given in heliocentric coordinates.

For the input data of the orbit determination, two approaches have been tried. The first one uses the initial state vector recorded by the ground cameras. The second integrates the

trajectory of the meteoroid backwards and uses the state vector at a height of 1000 km as the input data. The integration is done assuming that above 100 km height the atmosphere is not significant to the problem and therefore neglected.

Independently of the approach that is followed, the conversion of the state vector to heliocentric coordinates is the same.

The conversion of the position to heliocentric coordinates is done following the methodology explained in the section 4.3.

The velocity, on the other hand, requires some corrections before it is converted to heliocentric coordinates:

1. The observed velocity vector is corrected with the Earth's rotation velocity. The Earth's rotation velocity is given by:

$$v_E = 2\pi|\vec{r}|\cos\varphi/(24 \cdot 3600) \tag{27}$$

where φ is the geocentric latitude of the initial position and r is the position of the meteoroid in ECEF. The corrected velocity vector is given by:

$$\begin{aligned} v_{c_x} &= v_x - v_E \sin\lambda \\ v_{c_y} &= v_y + v_E \cos\lambda \\ v_{c_z} &= v_z \end{aligned} \tag{28}$$

where λ is the geocentric longitude and $\vec{v}$ the input velocity.

2. The velocity is corrected to the Earth's gravity in order to obtain the geocentric velocity without the influence of the Earth's gravitational field. The geocentric velocity is calculated through conservation of energy:

$$\frac{1}{2}m|\vec{v_c}|^2 - \frac{Gm_E m}{|r|} = \frac{1}{2}m|\vec{v_g}|^2 - \frac{Gm_E m}{r_\infty} \tag{29}$$

where m is the mass of the meteoroid, m_E the mass of the Earth and v_g the geocentric velocity without the influence of the earth's gravity (r_∞). If we isolate the geocentric velocity, the equation is as follows:

$$v_g = \sqrt{\frac{|v_c|^2}{2} - \frac{G}{|r|}} \tag{30}$$

with the same direction of the velocity corrected with the Earth's rotation v_c [50].

With the velocity corrected, the conversion to heliocentric coordinates is also carried out using the transformations defined in section 4.3.

5.3 Orbital elements determination from state vectors

Once the state vector (r,v) of the meteoroid in heliocentric coordinates is calculated, the orbital elements can be easily determined. The methodology followed to obtain the Keplerian elements can be found in [48] and the code has been provided by David de la Torre, professor in the UPC:

1. Calculate the radial velocity:
$$v_r = \frac{r \cdot v}{|r|} \tag{31}$$

2. Calculate the specific angular momentum:
$$h = v \times v \tag{32}$$

3. Calculate the inclination:
$$i = \arccos \frac{h_z}{|h|} \tag{33}$$

4. Calculate the node line vector:
$$N = \hat{k} \times h \tag{34}$$
where $\hat{k}$ is the unitary vector pointing in the z direction.

5. Calculate the ascending node:
$$\Omega = \begin{cases} \arccos \frac{N_x}{|N|} & (N_y \geq 0) \\ 360^\circ - \arccos \frac{N_x}{|N|} & (N_y < 0) \end{cases} \tag{35}$$

6. Calculate the eccentricity vector:
$$e = \frac{1}{\mu}\left[\left(v^2 - \frac{\mu}{|r|}\right)r - |r|v_r v\right] \tag{36}$$
the magnitude of the eccentricity vector |e| is the eccentricity.

7. Calculate the argument of the perigee:

$$\omega = \begin{cases} \arccos \frac{N \cdot e}{|N||e|} & (e_z \geq 0) \\ 360^\circ - \arccos \frac{N \cdot e}{|N||e|} & (e_z < 0) \end{cases} \tag{37}$$

8. Calculate the true anomaly:

$$\theta = \begin{cases} \arccos \frac{1}{|e|}\left(\frac{h^2}{\mu|r|} - 1\right) & (v_r \geq 0) \\ 360^\circ - \arccos \frac{1}{|e|}\left(\frac{h^2}{\mu|r|} - 1\right) & (v_r < 0) \end{cases} \tag{38}$$

9. Calculate the semi-major axis:

$$a = \frac{h^2/\mu}{1 - e^2} \tag{39}$$

6 Numerical Model

This program is designed to calculate the trajectory of meteors entering the atmosphere with the purpose of calculating the approximate coordinates where the meteor hits the ground and obtaining the keplerian orbital elements around the sun of the meteor. That is done using an integration of the acceleration and mass equations of the meteor, which is considered as a point of mass. These equations take into account all the physical concepts mentioned and studied in Section 4.

6.1 Input data

The input data of the code consists on the initial conditions of mass, position and velocity of the meteoroid, its initial physical properties and the date-time of the recording of the meteor. The input physical properties of the meteoroid are:

- Ablation coefficient ($s^{-2}m^{-2}$)
- Shape density coefficient (MKS)
- Strength of the parent fragment (Pa)
- Exponential strength scaling parameter α

6.2 Algorithm for the simulation

The algorithm of the numerical code is schematized in Figure 24:

The simulation starts integrating the parent fragment. In every time step it checks if a condition to stop the integration is met: mass equals zero, ground impact or stagnation pressure greater than the strength of the fragment. If the mass is equal to zero or the fragment has reached the ground, the integration stops and the code stores the data of position, velocity, mass and time. On the other hand, if the fragmentation criteria is met, the parent fragment is divided into child fragments. Then, the velocities, masses and strengths of each child fragment are calculated, and each child fragment is integrated individually in the same way as

the parent fragment. This is achieved by means of a recursive function, which calls the integration function. If a fragmentation occurs, it calls itself again for each fragment. In the end, the code allows for multiple fragmentation using this recursive function that calls itself again and again (See Annex 1, section 1.5).

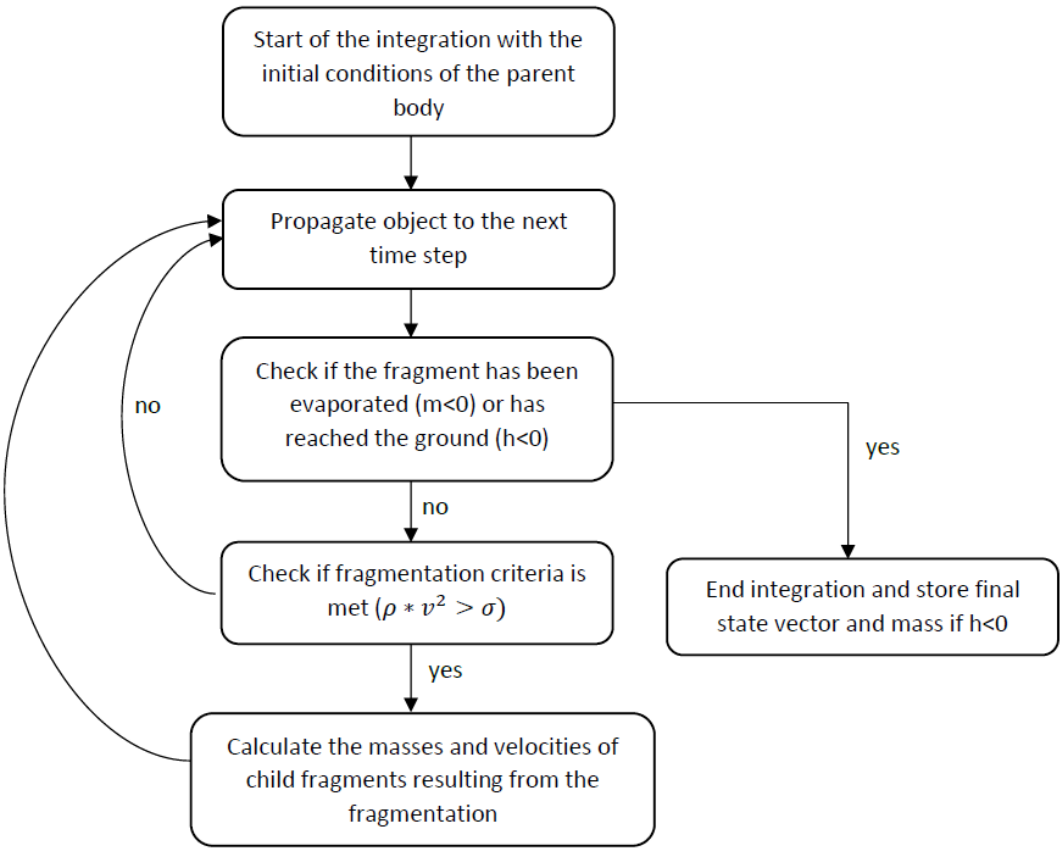

Figure 24: Schematic resolution algorithm of the simulation.

6.3 Differential equations

In section 4, all the physical models that the numerical code takes into account are explained individually, obtaining equations of velocity, mass, and position in respect to time. Grouping all these equations, the following set of differential equations is obtained:

$$\frac{d\vec{r}}{dt} = \vec{v} \tag{40}$$

$$\frac{d\vec{V}}{dt} = -K\rho_a m^{-1/3} v^2 \frac{\vec{v}}{|v|} - G\frac{M_T}{|r|^2} - 2\Omega_E \times \frac{\vec{r}}{|r|} - \Omega_E \times (\Omega_E \times r) \tag{41}$$

$$\frac{dm}{dt} = -K\rho_a \sigma m^{2/3} |v|^3 \tag{42}$$

As commented in the sections above, these equations are referenced to the ECEF coordinate system.

Equation 40 represents velocity of the meteoroid (differential equation of the position respect time) and is created in order to have a system of equations of first order, given that the acceleration is the second derivative of the position.

Equation 41 represents the acceleration of the meteoroid. The first part of the equation represents the drag force, and it is the same as Equation 13. The direction of the drag goes in the opposite direction to the velocity and is defined by the unitary vector $\frac{\vec{v}}{|v|}$. The second part of the equation represents the acceleration caused by the gravity, and is also the same as Equation 8. The direction of the gravity is always pointing to the Earth's center of mass and is defined by the unitary vector $\frac{\vec{r}}{|r|}$. Finally, the third and the fourth parts of the equation are the Coriolis force and the centrifugal force, respectively.

Equation 42 represents the rate of mass loss of the meteoroid, this equation is exactly the same as Equation 19 with the difference that now is dependent of the other equations.

For the integration the equations are decomposed into the axes of the ECEF coordinate system:

$$\frac{dx}{dt} = v_x \tag{43}$$

$$\frac{dy}{dt} = v_y \tag{44}$$

$$\frac{dz}{dt} = v_z \tag{45}$$

$$\frac{dv_x}{dt} = -K\rho_a m^{-1/3}|v|v_x - G\frac{M_T}{|r|^3}x + 2\Omega_E v_y + \Omega_E^2 x \tag{46}$$

$$\frac{dv_y}{dt} = -K\rho_a m^{-1/3}|v|v_y - G\frac{M_T}{|r|^3}y - 2\Omega_E v_x + \Omega_E^2 y \tag{47}$$

$$\frac{dv_z}{dt} = -K\rho_a m^{-1/3}|v|v_z - G\frac{M_T}{|r|^3}z \tag{48}$$

$$\frac{dm}{dt} = -K\rho_a \sigma m^{2/3}|v|^3 \tag{49}$$

6.4 Integrator

The integration is done using the ode45 function, which is a solver which is based on an explicit Runge-Kutta (4,5) formula, the Dormand-Prince pair. It is a single-step solver – in computing y(tn), it needs only the solution at the immediately preceding time point, y(tn-1) [51].

An important parameter of the integration is the precision of the ode. In the case of the Matlab's ode45 the precision is controlled by two parameters [52]:

- **'AbsTol'**: Absolute error tolerance. It is the limit beyond which the solution ceases to be important and is therefore not guaranteed to be correct.
- **'RelTol'**: Relative error tolerance. This parameter calculates the error relative to the magnitude of each component. In other words, it controls the number of correct digits of each component.

At each step of integration, the solver estimates the error (e) of each component (i). For the result of each step to be acceptable, the error must meet the tolerance:

$$|e(i)| \leq max(RelTol * abs(y(i)), AbsTol(i)) \tag{50}$$

To determine suitable values of 'RelTol' and 'AbsTol', several simulations without fragmentation have been carried out for different error values. In Figures 25, 26, 27 the error is plotted against the values of 'RelTol' and 'AbsTol'. As shown in the figures, the error becomes almost zero near values of 10^{-8}. Therefore, the chosen values of 'RelTol' and 'AbsTol' is 10^{-8}.

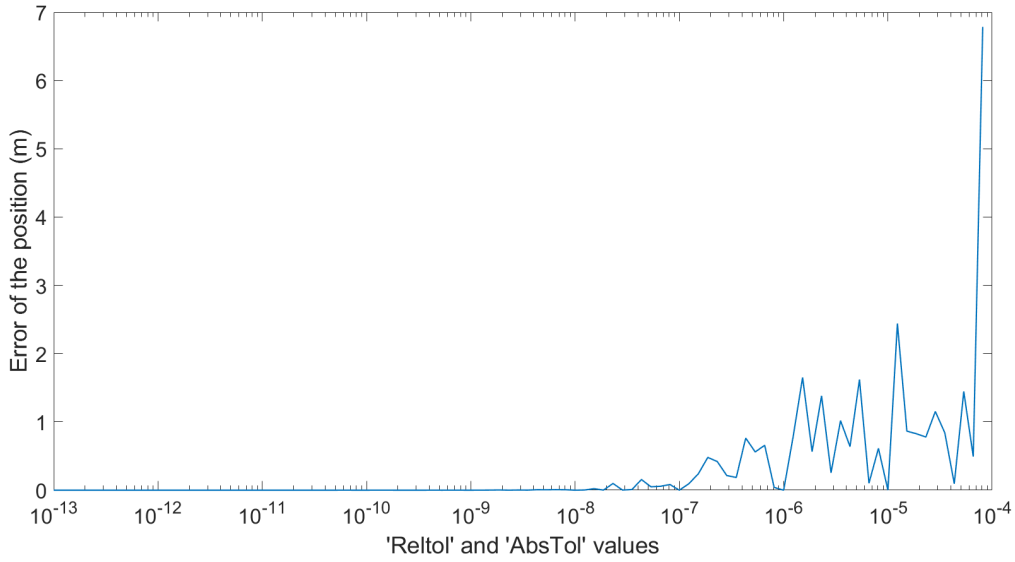

Figure 25: Error of the position.

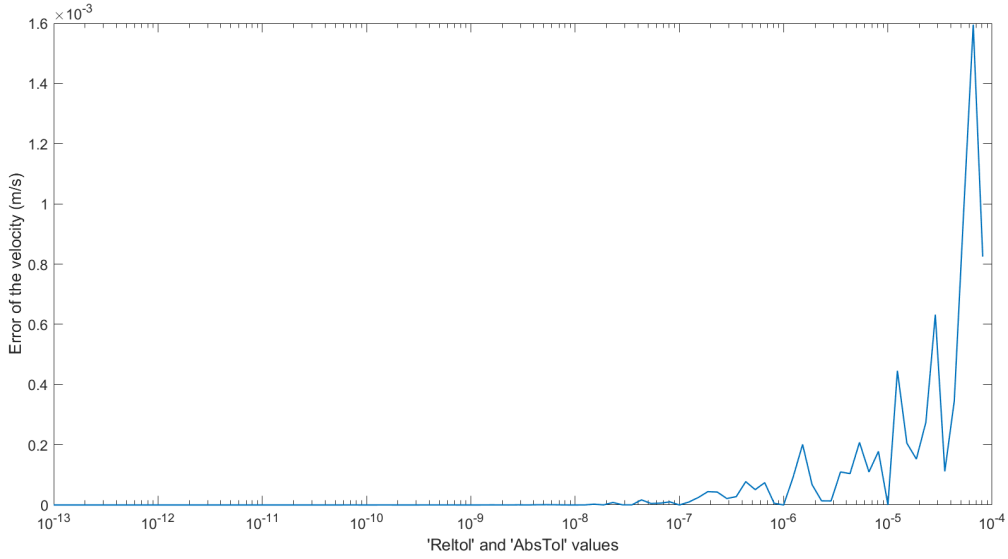

Figure 26: Error of the velocity.

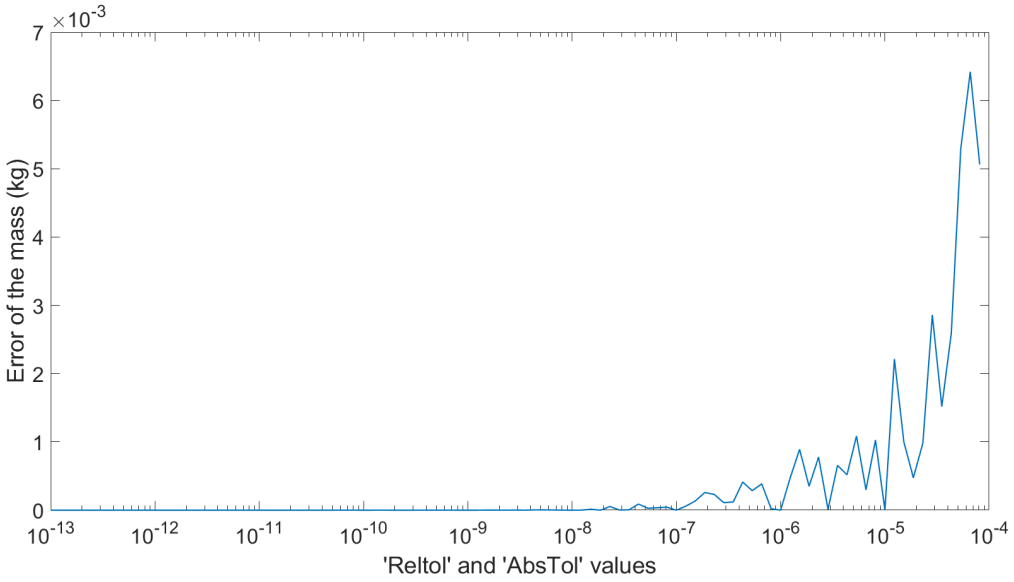

Figure 27: Error of the final mass.

7 Results and Discussion

In order to test the model, the code is applied to the case of the Hamburg meteorite fall, that was photographed and later successfully found on Michigan in 2018, and the orbit is compared with the one determined in [30], a paper dedicated to the study of the trajectory and orbit of the meteorite. The physical properties of the meteorite are also extracted from this article.

Although the Hamburg meteorite was successfully recorded and found, many parameters of the simulation, such as wind and meteorite properties, still have some uncertainty. That is why a sensitivity study is also carried out to determine the importance of these parameters for this meteorite and for future studied meteorites.

7.1 Hamburg meteorite

The Hamburg meteorite fall occurred on the 17 of January of 2018 close to Ann Arbor, Michigan. The meteor was widely seen in 7 U.S. states and the Canadian province of Ontario. A total of 26 fragments were recovered, mostly from frozen lakes. The meteorites found belong to the chondrite group.

Although the all sky cameras of the Southern Ontario Meteor Network and NASA All Sky Fireball Network were mostly overcast at the time of the fall, one camera in Oberlin, had a partial clear sky and was able to record the fireball through thin clouds. Apart from that, there were 27 geolocated casual video recordings, but only four of them were selected because of its direct view of the fireball and fixed recording positions, which made it possible for the astrometric calibrations [30]. From these four casual recordings the initial positions and velocities were calculated. This data is summarized in Table 3.

The total energy of the fireball was $8.4 - 28 \times 10^9$ J, which corresponds to an initial mass ranging from 60 to 225 kg or a diameter between 0.3 and 0.5 m. As a first approximation the mass of the parent fragment is set to 150 kg.

Apparently, the first minor fragmentation occurred at 0.3 MPa, and although evidence is not conclusive, it is the stagnation baseline pressure given to the parent fragment [30].

	Beginning	End
Height (km)	83.02 ± 0.01	19.73 ± 0.01
Latitude (N)	43.320 ± 0.0001	42.451 ± 0.0001
Longitude (W)	83.567 ± 0.0005	83.857 ± 0.0002
Slope (º)	66.14 ± 0.29	
Azimuth of the radiant (º)	121.56 ± 1.2	
Velocity (km s^{-1})	15.83 ± 0.05	
Time (UT)	01h 08m 29s	01h 08m 34s

Table 3: Position and velocity of the fireball at the start and end points of the recordings [30].

The exponential strength scaling parameter (α) used is taken from [53], which ranges the value from 0.1 to 0.5 for chondrite meteoroids. As a first approximation the scaling parameter is set to 0.25.

The shape-density coefficient and the ablation coefficient are 0.0046 (MKS) and 0.004 $s^{-2}km^{-2}$ respectively. These values are estimated in [30] following the approach of Ceplecha and Revelle [13].

In Figure 28, the velocities of the wind used for the simulation are plotted as a function of the height, which are obtained with the wind model described in Section 4.8.

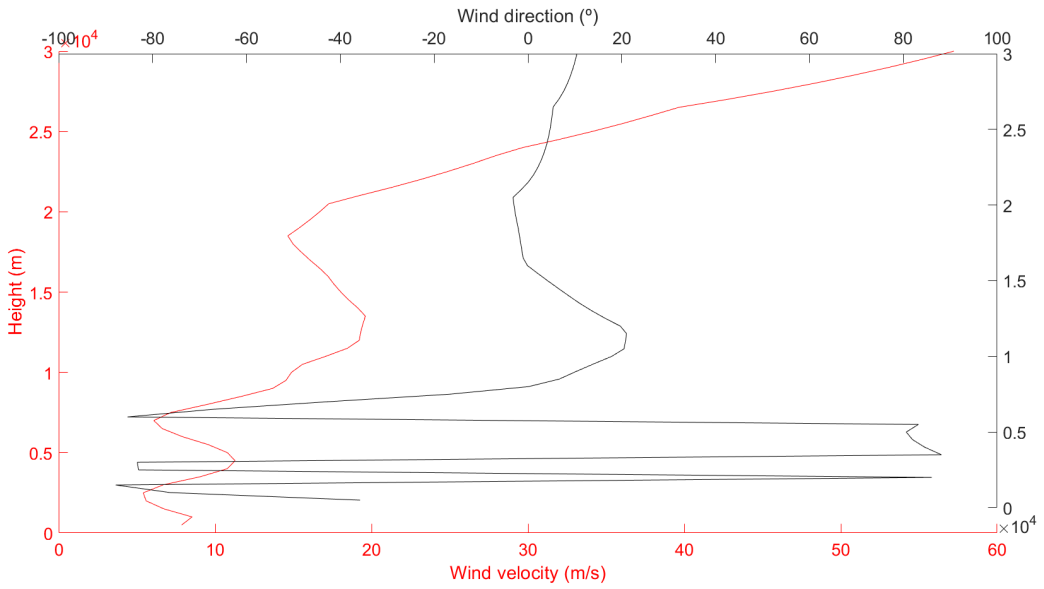

Figure 28: Wind conditions at the time of the fall

Using these values, the simulation is carried out. Given that the fragmentation is somewhat random, a total of 100 simulations have been carried out in order to obtain average values and thus ensure that the simulation is not an exceptional case.

Trajectory

Figures 29 to 33 describe the trajectory of the meteoroid in one of the simulations. In the first seconds of the simulation, which correspond to the period of intense ablation, most of the deceleration and loss of mass of the meteoroid occurs. The figure shows how the speed decreases from 15 km/s to several meters per second in these firsts seconds, until reaching a point where the velocity stabilizes and the meteoroid enters in a regime of free fall.

In this regime, the lateral velocity is almost null and the meteoroid falls almost vertically. In Figures 30 and 31 it can be apreciated a small variation in the values of longitude and latitude, which corresponds to the effect of the wind, that changes its direction as a function of the height. That is why this curve makes the coordinates change both up and down.

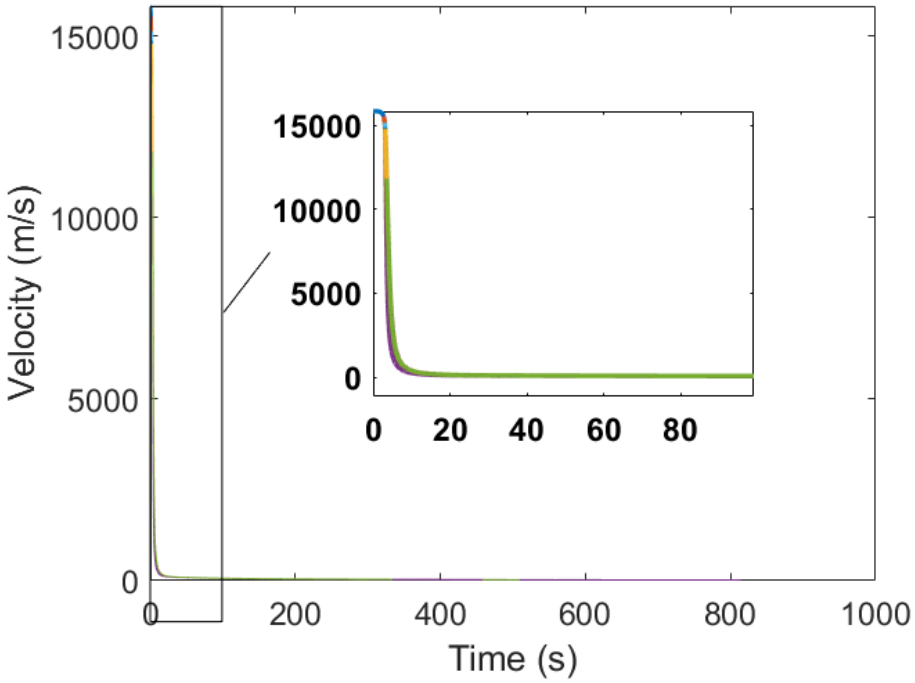

Figure 29: Velocity of the fragments as a function of the time.

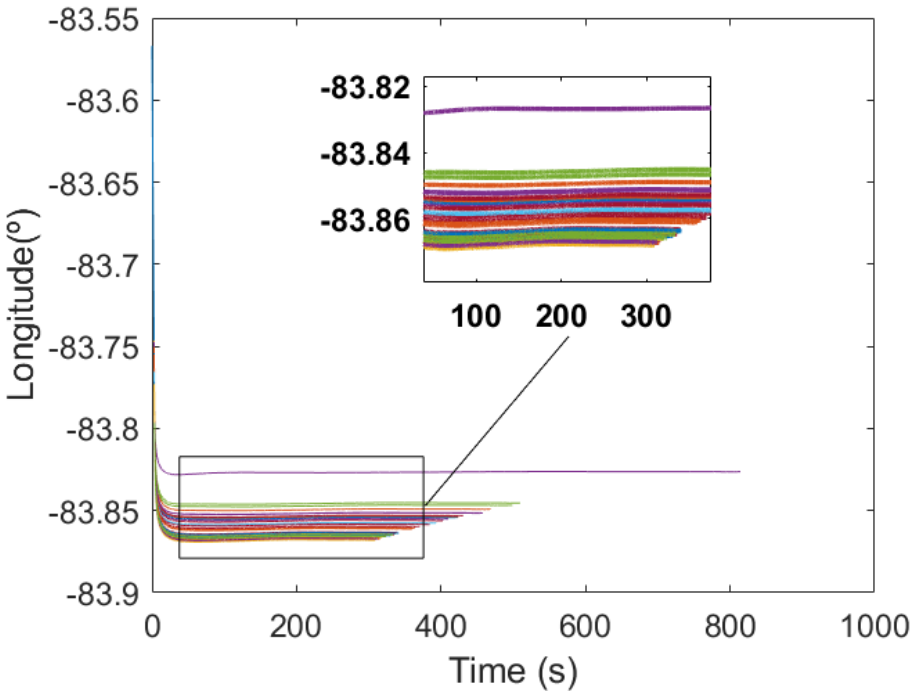

Figure 30: Longitude of the fragments as a function of the time.

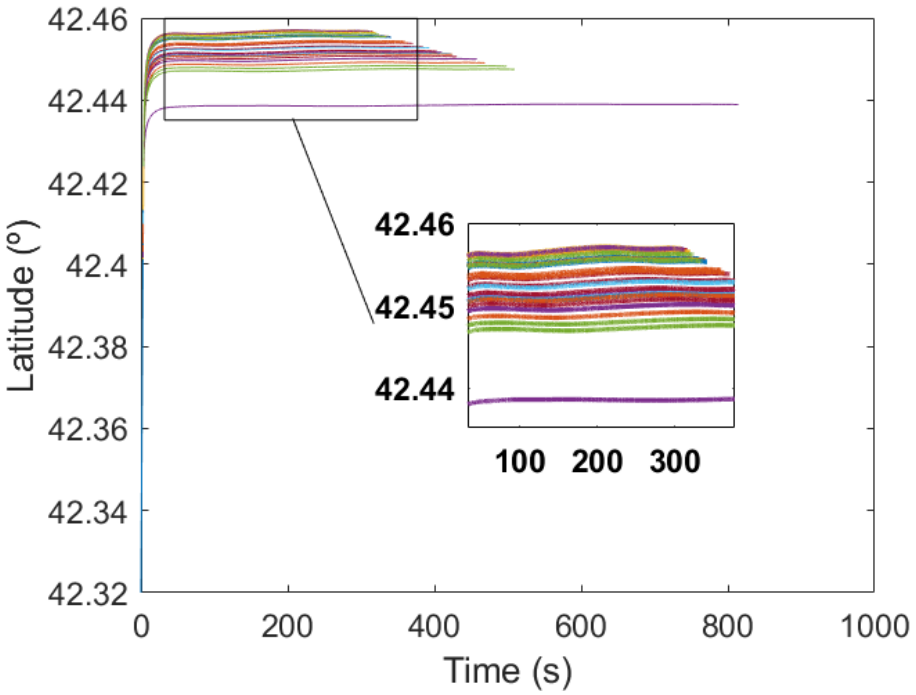

Figure 31: Latitude of the fragments as a function of the time.

The fragmentation of the body occurs in the first seconds of the trajectory, where the velocity is still high, and from there, once the velocity is low enough, the mass of the fragments slowly decreases.

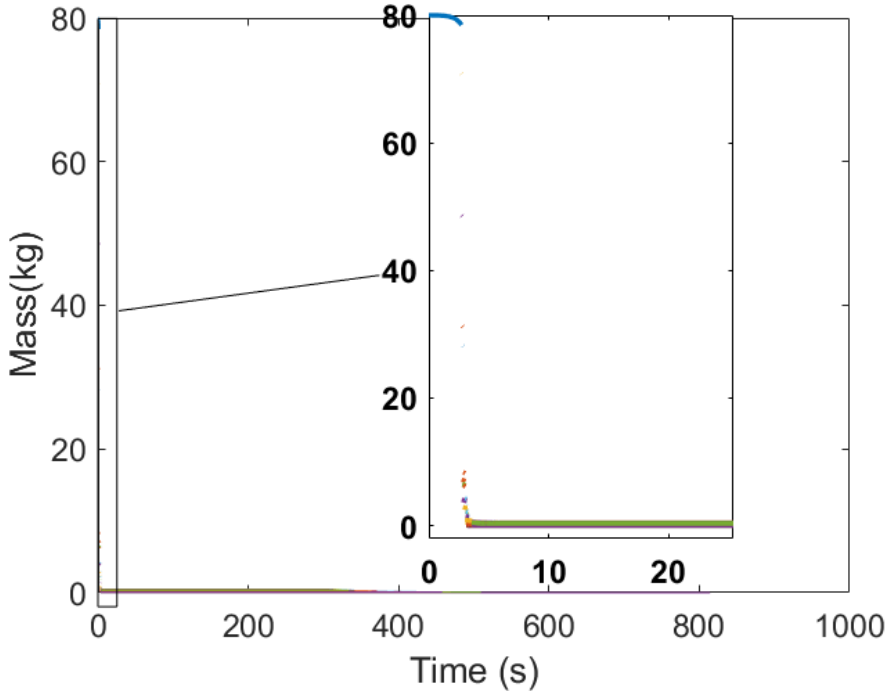

Figure 32: Mass of the fragments as a function of the time.

Finally, the height of the fragments decreases almost vertically during the regime where the velocities are high and from there it decreases far more slowly. If the air density was constant, this final regime would be a straight line, and the terminal velocities would be achieved, but as the density increase, the deceleration becomes bigger and that explains the slight curve on the height after the first seconds (see Figure 33).

The difference in the fall time duration of the fragments is directly related to its mass. Fragments with bigger mass have more momentum and a smaller deceleration (see Equation 41), and therefore they reach the ground in less time.

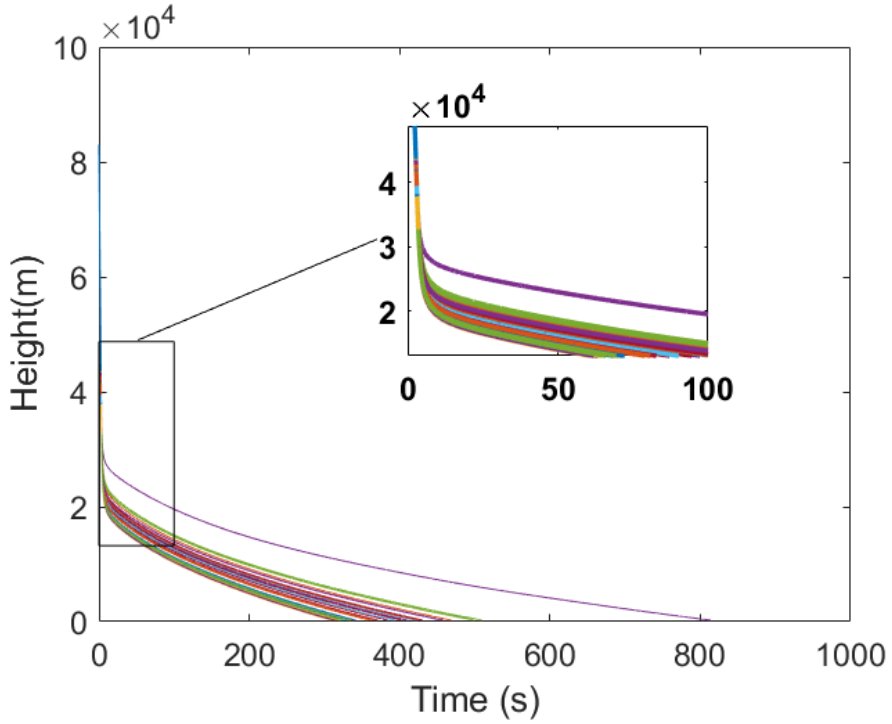

Figure 33: Height of the fragments as a function of the time.

Impact points

A total of 26 fragments were found. In the table 4, all the fragments are listed with their respective coordinates and masses.

The largest fragment found weights 102 g, and in total they sum up to a weight smaller than 1 kg.

In comparison, in table 5 the average values of the simulation are exposed. The average impact point is plotted as a red dot in Figure 34. The average number of fragments using these initial conditions and meteorite properties is quite high, and does not correspond to the reality of the case. The reason there are that the simulation results in this large number of fragments can be due to many factors. As later seen on the sensitivity study, almost every studied parameter makes the number of fragments change, but the only one that does not affect significantly neither the final mass or the locations of the fragments is the cloud mass in each fragmentation.

Date	Finder	Location	Mass (g)	Notes
January 18, 2018	T. Slisher	42.4485996, −83.8358445	12	Found on lake
January 18, 2018	T. Licata	42.4488509, −83.8385039	15.83	Found on lake
January 18, 2018	B. Wolfe	42.4490422, −83.8483335	26	Found on lake
January 20, 2018	A. Licata	42.4502360, −83.8589170	0.9	Multiple specimens
January 20, 2018	B. Barnibo	42.4362000, −83.7983910	3	Found on lake
January 20, 2018	E. Licata	42.4351030, −83.7943220	0.301	Found on lake
January 27, 2018	T. Licata	42.4508390, −83.8226400	10.43	Found in wooded area
January 18, 2018	D. Landry	42.4541500, −83.8641120	20	AMS
January 19, 2018	G. Barger	42.4533040, −83.8608600	11	AMS
January 19, 2018	L. Janes	42.4512560, −83.8603470	20	AMS
January 26, 2018	R. Matthews	42.4507690, −83.8589820	2	AMS
January 26, 2018	L. Matthews	42.4506450, −83.8588070	1	AMS
January 18, 2018	A. Larry	42.4484540, −83.8590680	17.5	AMS
January 18, 2018	Resident	42.4500280, −83.8542220	~60	Witnessed by Brandon Weller, found on land
January 18, 2018	B. Weller	42.4520280, −83.8504440	59.4	AMS
January 18, 2018	R. Ward	42.4511390, −83.8476390	102.6	Largest found fragment—Witnessed by Brandon Weller
January 18, 2018	L. Atkins	42.4488730, −83.8386330	37	AMS
January 20, 2018	L. DeLanoy	42.4471920, −83.8276960	6.5	AMS
January 19, 2018	T.V.	42.4475530, −83.8359690	13.8	
January 19, 2018	T.V.	42.4475140, −83.836789	12.6	
January 19, 2018	T.V.	42.4470070, −83.8384670	11.5	
January 22, 2018	D. Grischke	42.4535890, −83.8560520	55.92	AMS
January 27, 2018	T. Licata	42.4478106, −83.8135184	0.2	Found on air field
January 28, 2018	T. Licata	42.4511370, −83.8532140	0.008	Found in baseball field
January 20, 2018	A. Moritz	42.4573020, −83.8473590	50	
January 18, 2018	Unidentified	42.4512560, −83.8560530	20.6	

Table 4: Documented Hamburg meteorite recoveries [30].

Currently the fragmentation model has as a condition that 50-99 % of the mass belongs to a first fragment, while the rest is distributed between the second fragment and the mass of dust. But if the meteorite being studied has a very loose structure, as the hamburg meteorite seems to have, this model may not be entirely accurate in terms of number of fragments since the mass of dust will always have a small percentage.

Longitude	-83.848º
Latitude	42.448º
Number of fragments	182
Final mass	0.0938 kg

Table 5: Average values of the simulation.

In the figure 34, the concentration of fragments is represented in different colours. From less to more, the colors range from blue to yellow to red. Most fragments are concentrated on the left side of the map, although the distribution is rather homogeneous for all impact points. They are also more concentrated in the middle of the trajectory line than on the sides. The

lateral displacement from the mean trajectory line is due to the lateral velocity that the child fragments gain in each breakup, which in any case is larger than 100 m.

On the mass of the meteorites, there is a clear relation between the terminal mass and the distance from the beginning of the trajectory. As seen in the figure, the fragments with more mass go further, following a distribution that resembles a rational function, since the term of mass is divided in the function of acceleration (see Equation 41). Therefore, in general, the further to the left of the map a fragment is, the more mass it has. This majorly fits in with the fragments found, although there are some exceptions of low-mass fragments found further away than what should be expected with the current model.

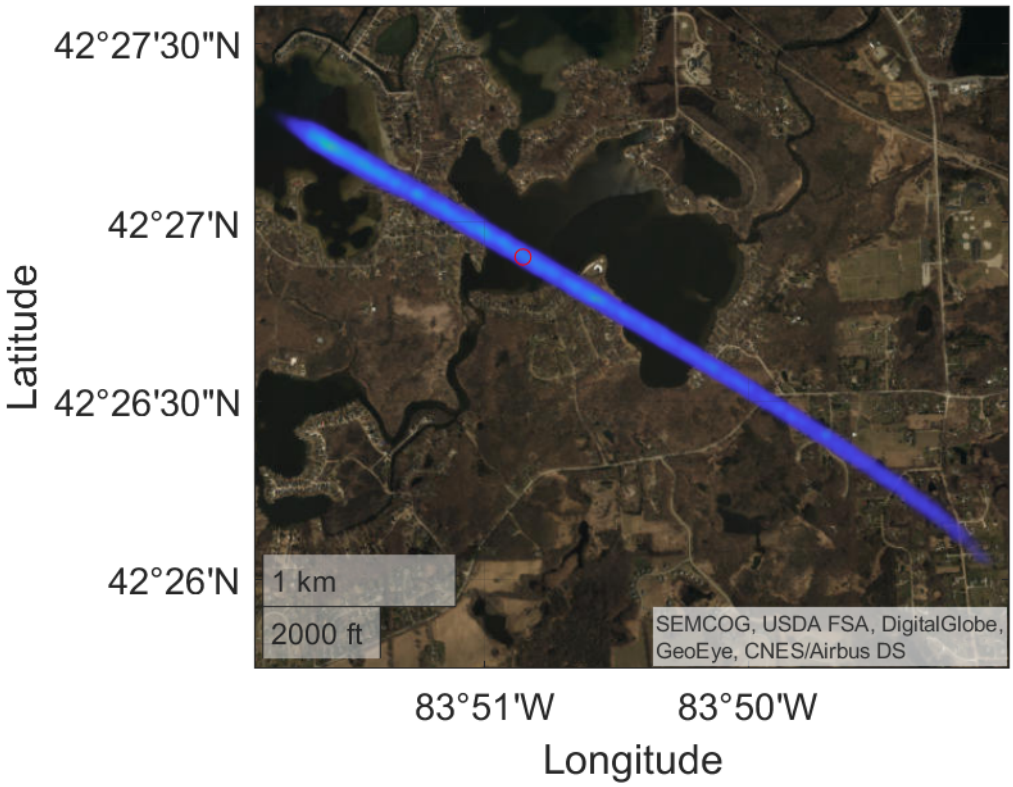

Figure 34: Density plot of the ground impact points of the simulation.

As far as the final coordinates go, the results of the simulation give coordinates quite similar to those of the recovered fragments (see Figures 34 and 35), although the smaller the mass is the more the results differ from reality. For masses of around 100 g the results are less than 200 m of radius from reality, but as the mass decreases, this radius becomes larger. This is probably

due to an imprecise wind model, since the lower the mass the more the body is affected by the wind, and therefore the more important a precise wind model becomes.

Figure 35: Coordinates of the recovered fragments of the Hamburg meteorite [30].

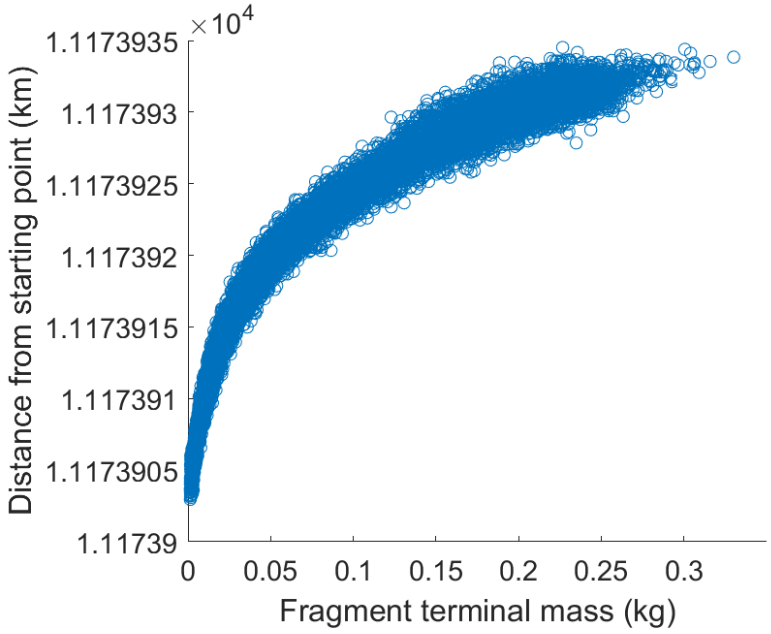

Figure 36: Distance from the beginning of the trajectory as a function of the terminal mass.

Orbit

The results of the meteoroid orbit calculation are compared with the results of the article [30], which are presumably correct (see Table 6).

	Backwards integration	Initial Recording	Brown et al. (2019) [30]
a [A.U.]	2.788	2.863	2.73 ± 0.05
i [°]	1.238	1.41	0.604 ± 0.11
e	0.6654	0.674	0.661 ± 0.006
ω [°]	211.161	211.037	211.65 ± 0.11
Ω [°]	295.997	296.041	296.421 ± 0.03
θ [°]	329.205	329.286	-

Table 6: Comparison of the orbital elements obtained with two approaches and the article of study.

The heliocentric orbit of the meteoroid prior to interaction with the Earth's gravitational field has been calculated in two ways. The first uses the velocity and initial position of the

meteoroid, i.e. the first position that was recorded and in the second, the position and speed are integrated backwards to 1000 km height assuming that the atmosphere is negligible after 100 km.

Both approaches result in a similar orbit, although the one that comes closest to the orbit calculated in [30] is the one made by backward integration. A possible explanation may be that both the velocity and the direction of the meteoroid are less influenced by the Earth's gravity in that case.

Even so, only the semi-major axis and eccentricity fall within the range calculated in [30]. In this article the orbit is calculated based on average coordinate and velocity of the trajectory, following the approach defined in [50], which differs from the method adopted in this study, and as a consequence the results vary. Overall, though, the orbit calculated in this study is very similar to the one calculated in the mentioned article.

7.2 Sensitivity study

Due to the high uncertainty in the multiple parameters that appear in the differential equations, a sensitivity study has been conducted to determine how and how much each parameter affects the simulation results. For each value of the parameters studied, 10 simulations have been carried out in order to obtain average values and thus generalize the randomness of the fragmentation model. Table 7 shows the base values and variations of these parameters, the range of which is discussed below. The sensitivity study is conducted only for the study of the trajectory, given that it is where these parameters affect the most.

	Baseline value	Variation
Initial strength of parent fragment	0.5 MPa	0.3-2MPa
Strength scaling parameter α	0.25	0.1-0.5
Shape-density coefficient	0.0046 (MKS)	0.0025-0.0105 (MKS)
Ablation coefficient	4e-9 $s^{-2}m^{-2}$	1e-9 - 8e-9 $s^{-2}m^{-2}$
Mass of parent fragment	60 kg	60-225 kg
Dust mass in each fragmentation	0-50 %	10-90 %
Number of fragments in each fragmentation	2	2-8

Table 7: Baseline values and variations of the parameters used for the sensitivity study.

In addition, to have a reference of the importance of the wind model, the wind speeds are multiplied by different factors and the implication of the wind interpolation is analyzed with respect to the files generated every 6 hours by [37].

Effect of the strength scaling parameter α

The strength scaling parameter determines the strength that the fragments have after each fragmentation. The greater the value of α, the greater the strength of each child fragment. As a consequence, the greater the scaling parameter, the lesser fragmentation events and the larger the final masses are (see Figure 38 and 37).

The value of α can be in the range between 0 and 1, but for meteoroids, values between 0.1-0.5 have been standardized based on published measurements and modeling conventions for stony bodies [53, 54]. However, these values are still subject to great uncertainty as it is not clear how well the meteoroid materials can be represented based on the small fragments recovered. That is why the range has been extended to 0.7 [40].

As α increases and the masses of the fragments increase, the impact points with the ground are also further located from the origin of the trajectory. That is because the fragments have more momentum and are more slowly decelerated (see Figure 39).

This shows that this parameter is indeed very important in the determination of the impact points, being a key factor in the determination of the size and number of fragments that reach

the ground.

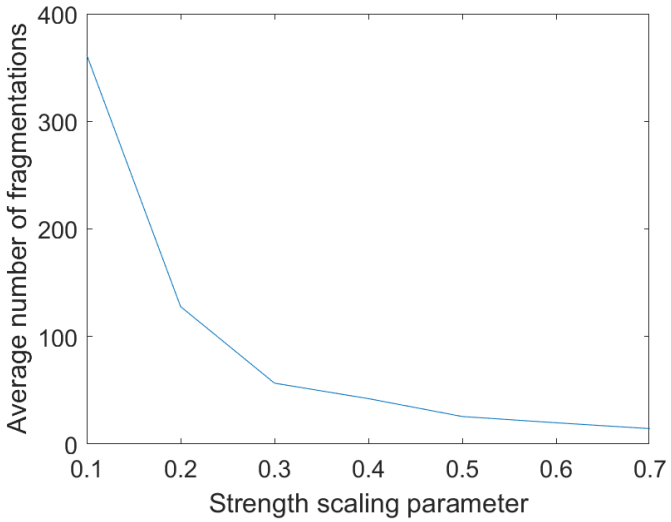

Figure 37: Variation of the number of fragmentation events with α.

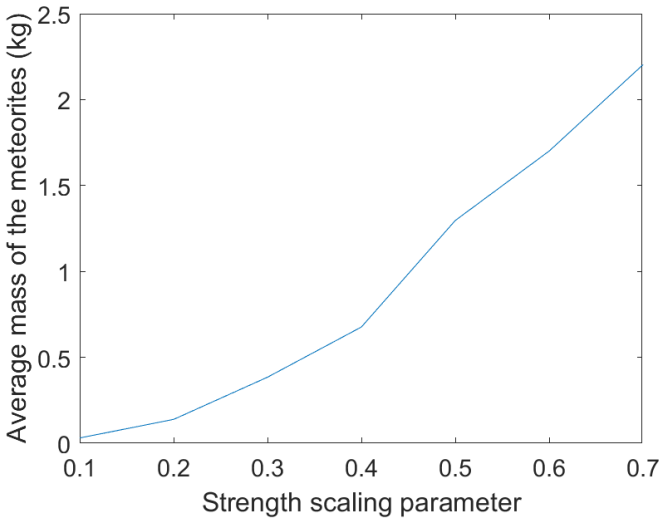

Figure 38: Variation of the final fragments mass with α.

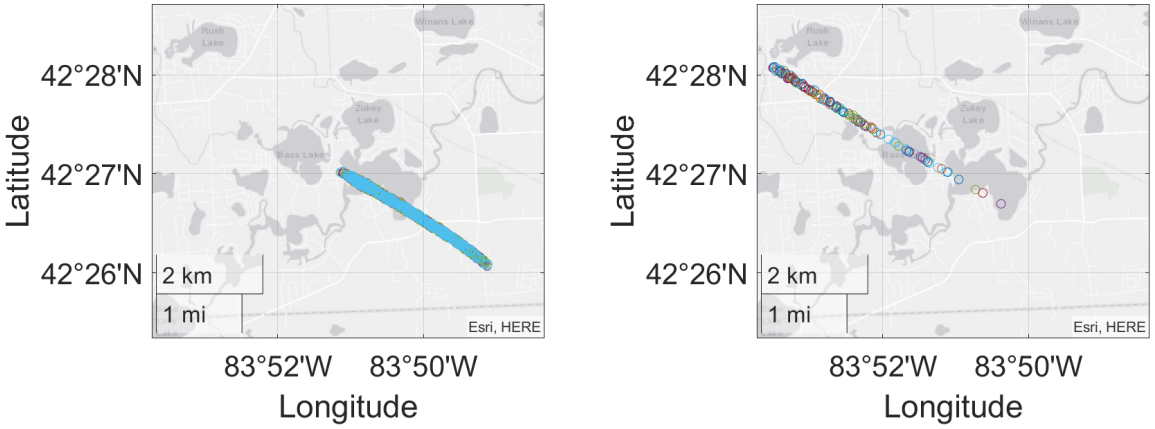

(a) $\alpha = 0.1$.

(b) $\alpha = 0.7$.

Figure 39: Impact points for different α.

Effect of the shape density coefficient

The shape density coefficient (K) is a parameter that appears in all the differential equations and defines how the meteoroid interacts with the incoming air, taking into account the shape, density and drag coefficient of the meteoroid. The larger the coefficient, the greater the deceleration and the ablation of the body (see Equations 41, 42). The range of K is chosen based on the values of similar chondritic meteorites of the type I, with K ranging from 0.0025 to 0.0105 [40].The baseline value being used is the same as the one estimated in [30].

As seen on Figures 40 and 41, as the coefficient increases, the number of fragments increases and their size decreases. That is because the larger the coefficient, the faster the body decelerates, so that it reaches small speeds faster and fragments less. As it fragments less, the average mass of the fragments increases.

Overall, this parameter does not change considerably the area of possible meteor impact, but it rather affects the number and size of the fragments, as they increase in mass with the shape density coefficient and decrease in number. The impact points are similar for all the values because the moment gained with higher masses is compensated by the increase in the drag force.

To sum up, the shape density coefficient affects in a great manner the size and number of the

meteorites, while the terminal coordinates are very similar for all the values.

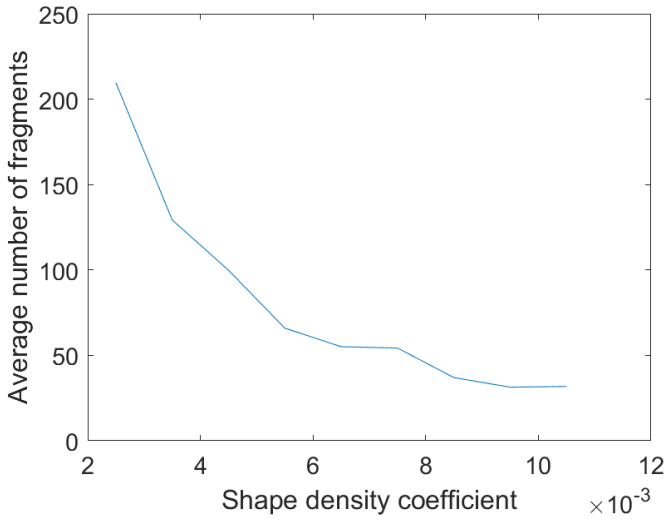

Figure 40: Variation of the number of fragmentation events with K.

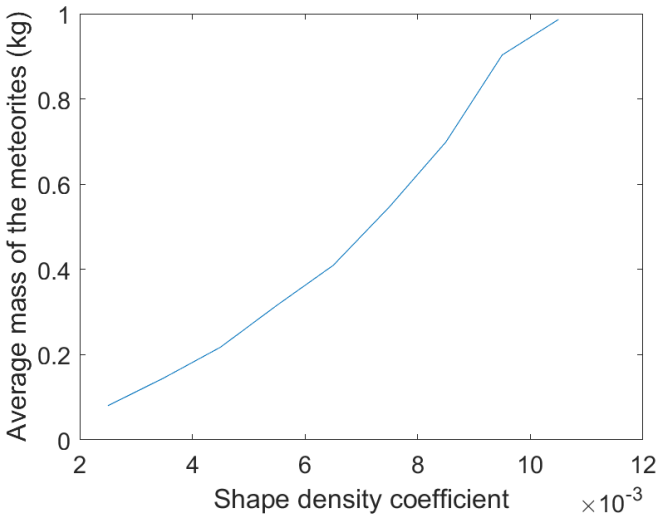

Figure 41: Variation of the final fragments mass with K.

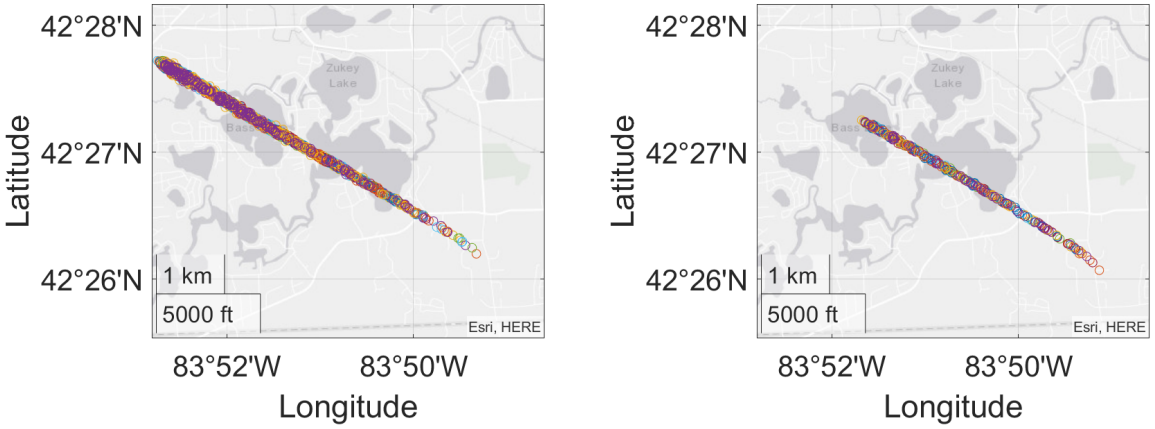

(a) $K = 0.0025$. (b) $K = 0.0105$.

Figure 42: Impact points for different K.

Effect of the initial mass

The initial mass is a very important parameter in determining the amount of mass that will impact the ground. The determination of mass is closely linked to the amount of energy emitted by the meteoroid. In this case the energy deduced from the recordings has a fairly wide range, so the mass has a high range of uncertainty. According to the article [30], the mass has a range of 60-225 kg.

For the sensitivity study, as a baseline value it has been decided to take the minimum, mainly for computational reasons, since the simulation time increases considerably with the mass.

Figure 43 and 44 show the effect of the initial mass has in the number and masses of the meteorite fragments. The greater the initial mass, the greater the number of fragments and their mass.

Although the tendency is to grow with the initial mass, the difference between the average terminal mass of the fragments with an initial mass of 60 kg and 225 kg is very small, only increasing by about 100 g, while the difference in the average number of fragments is more evident (from 55 to 115). This phenomenon can explained by the fact that the strength of the fragments depends deeply on how large they are (see Equation 21) and therefore, at high speeds, the meteoroid fragments multiple times until reaching a strength greater than the

aerodynamic pressure, which results in a very similar mass.

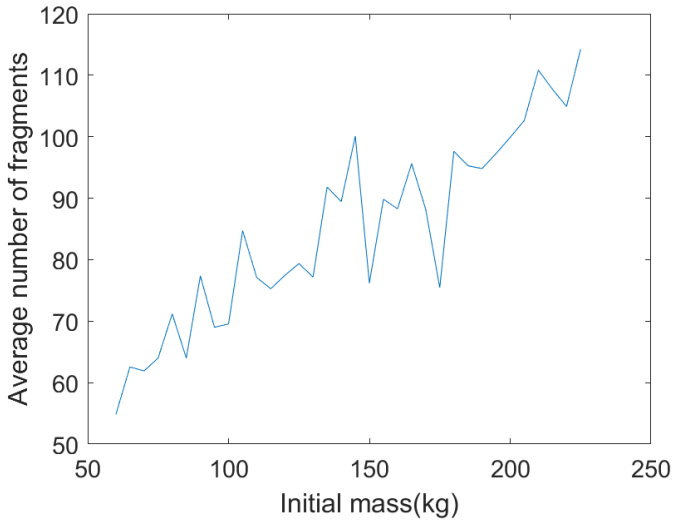

Figure 43: Variation of the number of fragmentation events with the initial mass.

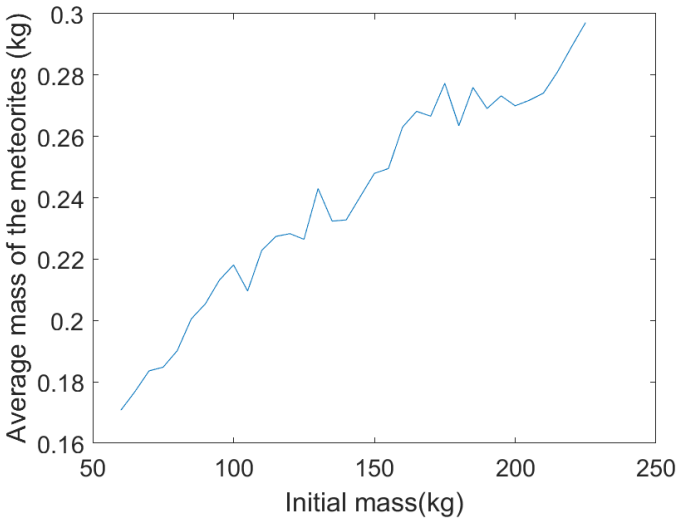

Figure 44: Variation of the final fragments mass with the initial mass.

As commented in section 7.1, for fragments of the same mass, the distances from the initial point of the trajectory are very similar, mostly due to the fact that they undergo a similar deceleration. That's why the initial mass doesn't greatly affect the impact coordinates of the meteorites.

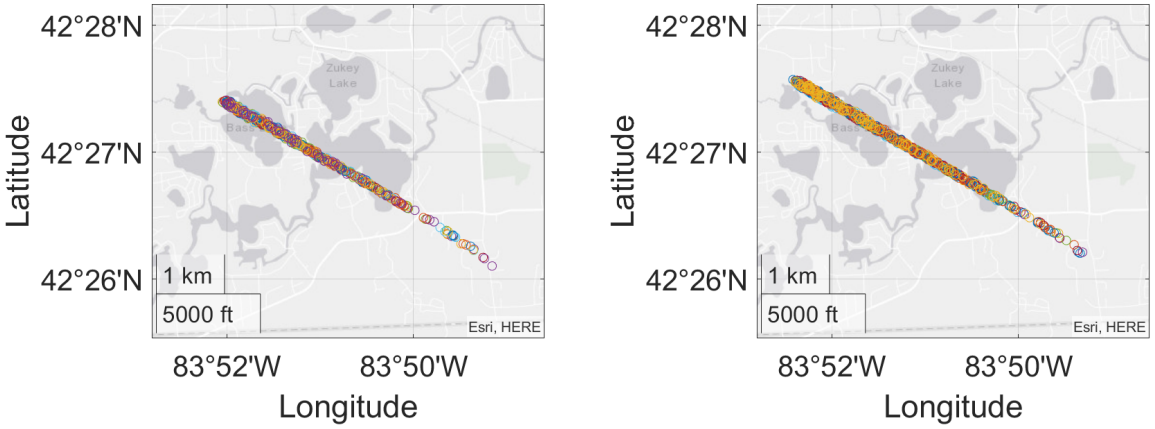

(a) $m = 60kg$. (b) $m = 225kg$.

Figure 45: Impact points for different initial mass.

Effect of the initial strength of the parent fragment

The initial strength of the meteoroid is one of the most important parameters in any fragmentation model, as it will define the point at which the body begins to break up. Although it is referred to as strength, it doesn't represent the physical strength of the material, but the pressure at which the body is assumed to fragment. That it why it is very difficult to propose a narrow range of values, specially for large bodies, because the structure can vary from a compact body to a conglomerate of fragments.

Using standard values of strengths based on previous observations [6], the range is defined between 0.3-2 MPa. The chosen baseline value is 0.5 MPa so that the strength is closer to the first value, but taking a slightly larger value in order to reduce the computational cost.

Similar to the effect of the strength scaling parameter, as the initial strength increases the number of fragments decrease and the final mass of the fragments increase. The tendency line of Figure 46 resembles an exponential function because of the scaling strength equation (Equation 21). As the results show, this is a very important parameter in the determination of the number and mass of the meteorites, but not only that, it also is key in determining the impact point of the fragments. Figure 48 shows that different initial strengths can lead to very different locations of the impact points, mainly due to the terminal masses of the fragments.

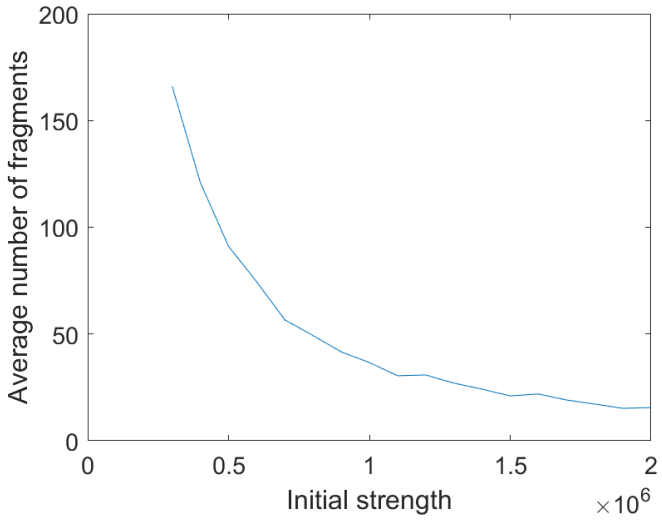

Figure 46: Variation of the number of fragmentation events with the initial strength.

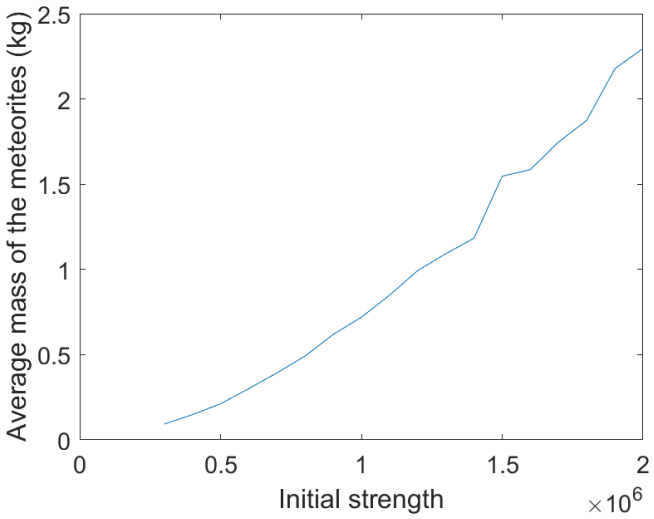

Figure 47: Variation of the final fragments mass with the initial strength.

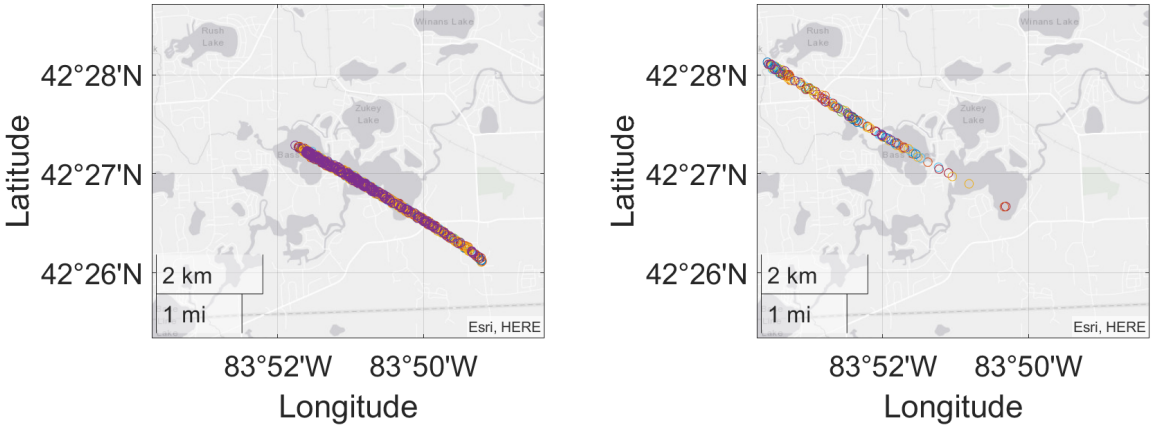

(a) $Strength = 0.3MPa$. (b) $Strength = 2MPa$.

Figure 48: Impact points for different initial strength.

Effect of the ablation coefficient

The ablation coefficient, as its name suggests, is the parameter that defines the rate of mass loss due to ablation and it significantly affects the final mass of the meteors.

Based on previously recovered meteorite data, the ablation coefficient has a approximate range of 1e-9 - 8e-9 $s^{-2}m^{-2}$ for chondritic type I meteorites [12] . The base value used for the sensitivity study is the same as estimated in the article [30] .

As could be expected, the mass of the final fragments decreases as the ablation coefficient increases. The number of fragments per simulation, on the other hand, is not affected by this parameter, since it does not affect either the speed or the parameters related to fragmentation (see Figure 49).

On the locations of impact of the fragments, a small variation can be appreciated between the maximum value simulated. As it can be observed in Figure 51, for smaller values, the fragments reach coordinates further away from the beginning of the trajectory. That is because the masses are greater and, as commented before, greater masses are less decelerated and reach further distances.

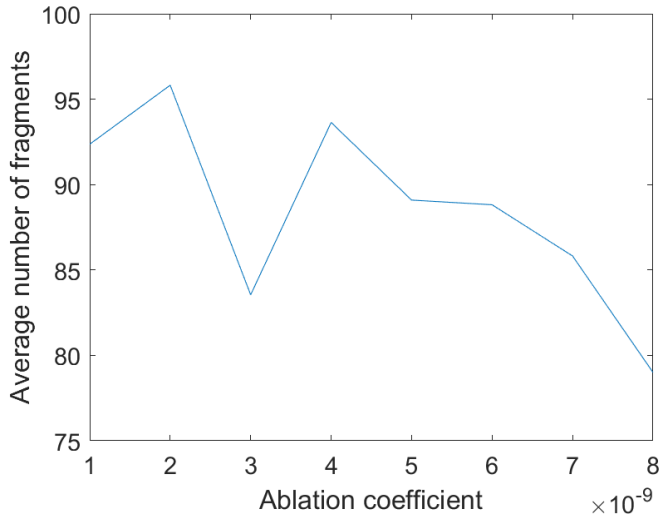

Figure 49: Variation of the number of fragmentation events with σ.

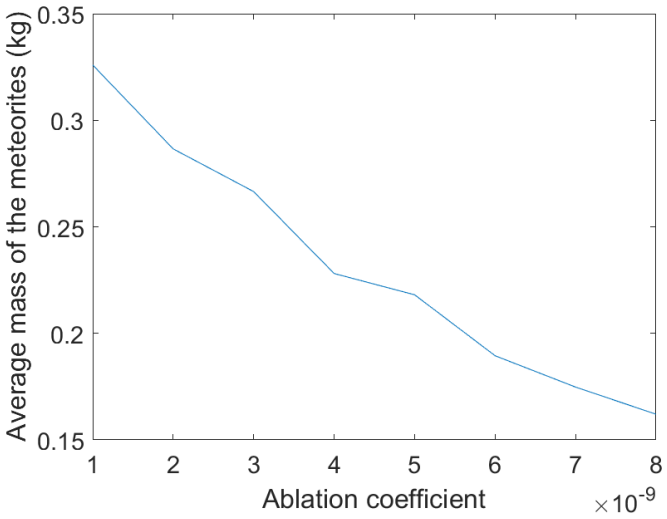

Figure 50: Variation of the final fragments mass with σ.

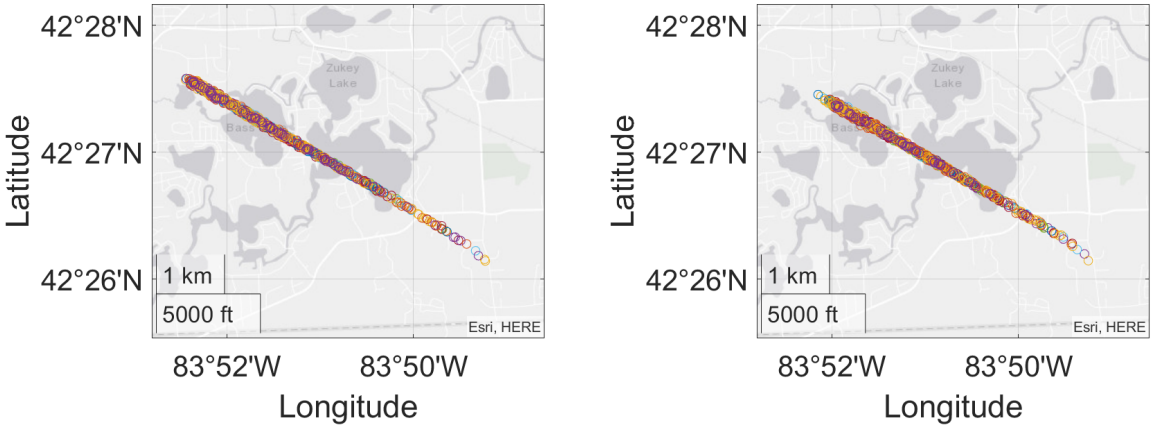

(a) $\sigma = 1e-9 s^{-2}m^{-2}$.

(b) $\sigma = 8e-9 s^{-2}m^{-2}$.

Figure 51: Impact points for different σ.

Effect of the dust mass per each fragmentation

The fragmentation model presented in this study proposes that the percentage of dust mass per fragmentation goes from 0 to 50 percent, although since it is random, the importance of this parameter is not appreciated. That is why, in order to study the sensitivity of the model to this parameter, the percentage of dust mass in each fragmentation is fixed and allowed to exceed the percentage of 50 percent. The range chosen for this parameter goes from 10 to 90 percent of the initial mass.

As the percentage of dust mass increases, the fragments resulting from each breakup are smaller and have a bigger strength. Therefore the number of breakups decreases and the final number of fragments is smaller (see Figure 52).

As for the mass or location of the fragments, no clear trend is observed, as the results are similar for all cases (see Figure 54).

Therefore, the amount of dust only significantly affects the final number of fragments, without varying the other results. This parameter should be varied according to the internal structure of the meteorite in question.

The fragmentation model implemented in the usually results in small dust mass percentages (50 -99 % of the mass goes to the first fragment and the rest is distributed between the second

fragment and the dust mass). That is why the number of fragments is so high. In this case a model with more freedom in the masses resulting from each fragmentation could be more suitable.

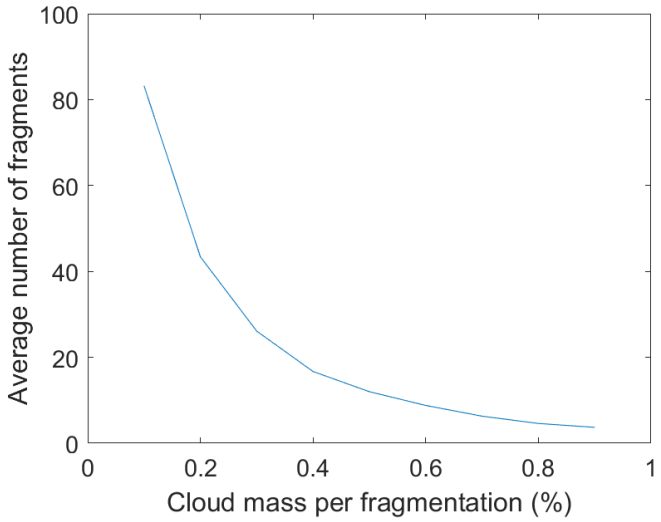

Figure 52: Variation of the number of fragments with the percentage of dust mass in each fragmentation.

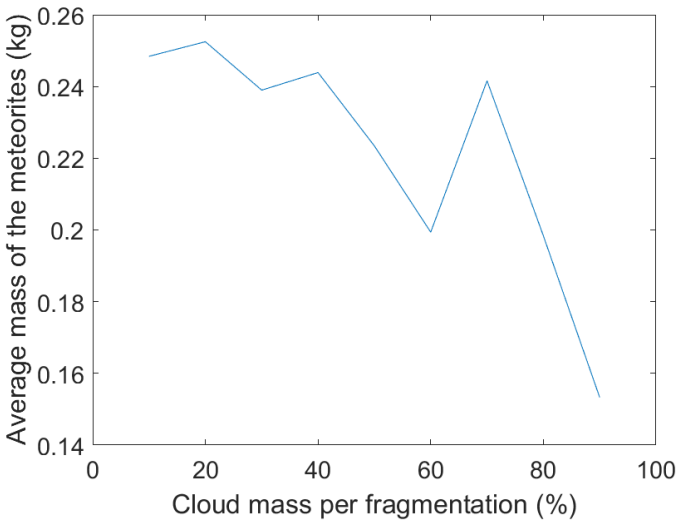

Figure 53: Variation of the final fragments mass with the percentage of dust mass in each fragmentation.

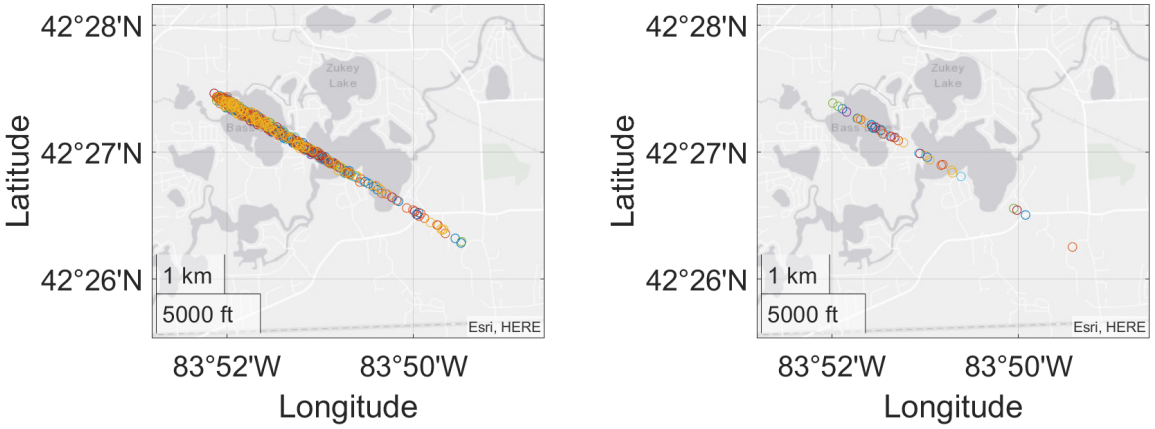

(a) 10%. (b) 90%.

Figure 54: Impact points for different percentages of dust mass in each fragmentation.

Effect of the number of fragments in each fragmentation

The fragmentation model proposed in this study assumes that in each fragmentation event the meteoroid splits in two fragments and a mass of dust. In order to test the effect of this hypothesis, simulations have been carried out with a number of fragments per fragmentation of a range of 2-8.

In the proposed model, the resulting masses of each fragment are distributed so that the first fragment occupies 50-99 % of the mass and the rest is distributed between the second fragment and the mass of dust This assumption is not considered here, given that if the number of fragments per fragmentation is larger, the secondary masses would be too small. Instead, the masses child fragments are calculated randomly and the the excess mass is attributed to the dust mass. For the case of 2 fragments per fragmentation, it will serve to compare this model of mass distribution with the model described in Section 4.9, that is the one applied to the main code.

As seen on Figure 55, as the number of fragments per breakup increases, the number of meteorite fragments also increases, given that more fragments are generated in each fragmentation. Also, this fragments are smaller and fragment less.

The mass of the meteorites also decreases, which is to be expected given that more fragments

are generated in each breakup (see Figure 56).

On the locations of the meteorite fragments, all the cases result in similar terminal coordinates, with the difference that for the more fragments per breakup, the more small fragments that are generated (see Figure 57).

Finally, if the results of this simulation with two fragments per breakup are compared with those of the model used in the other simulations, described in the section 4.9, it is concluded that both the size and the coordinates of the meteorite fragments are very similar for both cases, but that the final number of fragments is much lower with a random distribution of masses, mainly because the percentage of mass of dust is given more freedom. In the case of the Hamburg meteorite, this latter distribution better represents reality.

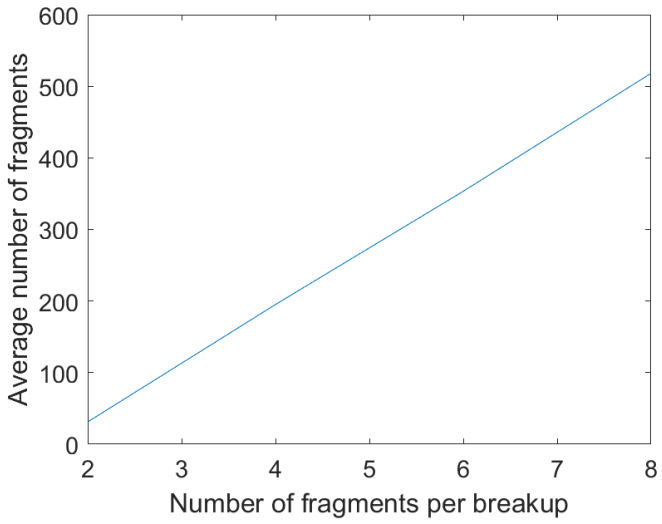

Figure 55: Variation of the number of fragments with the number of fragments per breakup.

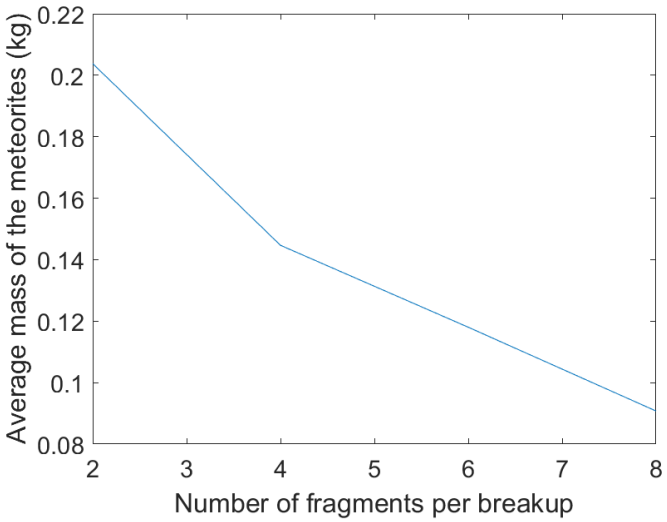

Figure 56: Variation of the final fragments mass with the number of fragments per breakup.

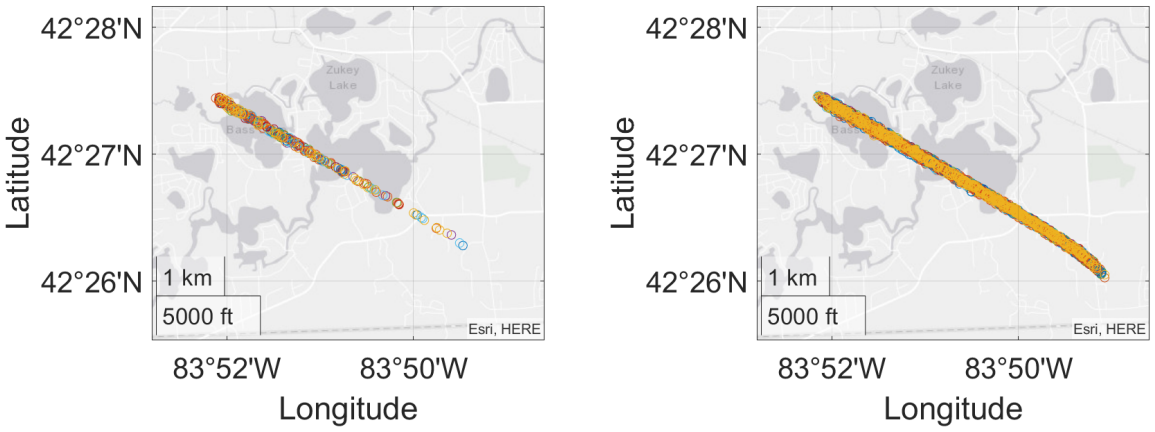

(a) 2 fragments per breakup.

(b) 8 fragments per breakup.

Figure 57: Impact points for different percentages of dust mass in each fragmentation.

Effect of the wind model

The wind is one of the most important aspects in this model. It affects the trajectory of the meteoroid during the free-fall regime, which can last several minutes. During this period the density increases exponentially and the speeds are equated to those of the wind.

In order to test the sensitivity and effect of the wind, the wind velocities are multiplied by factors ranging from 0 to 5 in all directions. Also, to check the importance of the interpolation

between the time of the wind files, which are 6 h apart, a simulation is carried out with both inputs of time.

From all the parameters studied in the sensitivity study, the wind is the only one that changes the mean line of the trajectory (see Figure 58). In this case, the simulation that best estimates the reality is when the wind velocities are multiplied by a factor of 4, and although it is not significant, this study provides an idea of the importance of finding a precise wind model.

Note that smaller fragments are more affected by the wind model, as it can be observed in Figure 58, where the further to the right the fragments are, i.e. the smaller they are, the more their position vary with the wind.

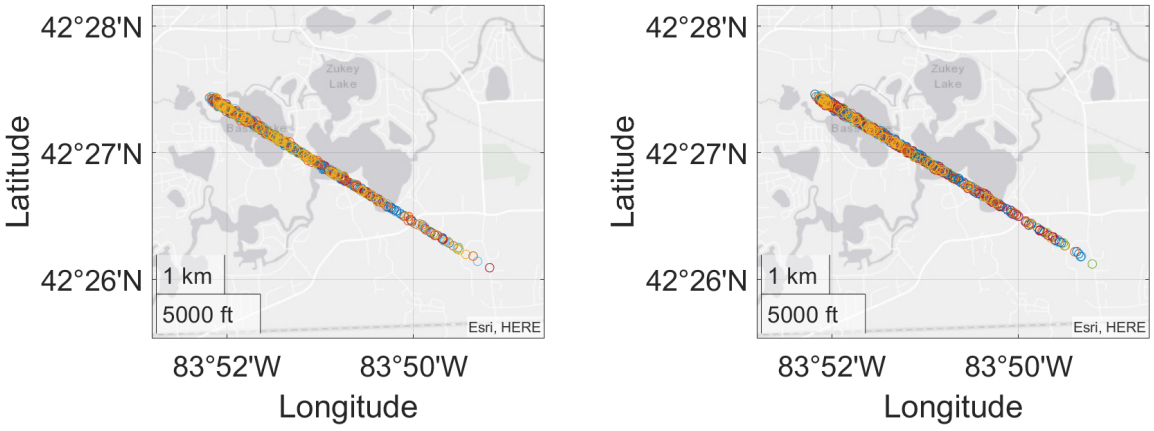

(a) Multiplier = 0.

(b) Multiplier = 0.5.

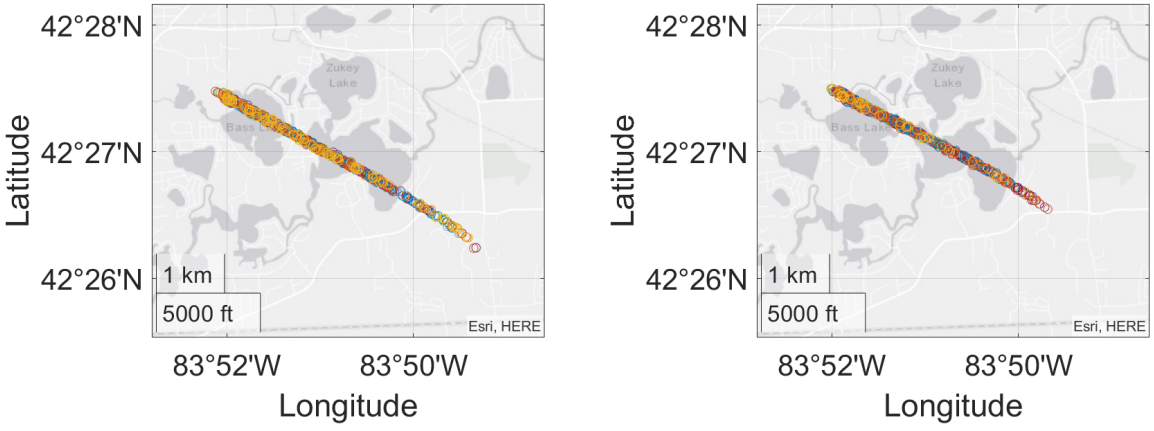

(c) Multiplier = 2.

(d) Multiplier = 4.

Figure 58: Coordinates of impact with the ground for different wind velocities.

Figure 59 shows the results of the simulation using the input files of the time corresponding to 00:00 and 06:00 (the time of the fall was 1:08). As it can be observed, there is no significant change between the two simulations, which means that in this case there is no serious error due to interpolation between times. If the wind were to change its behaviour significantly between the two hours, it would be necessary to study further when this change occurs and adapt the interpolation model accordingly.

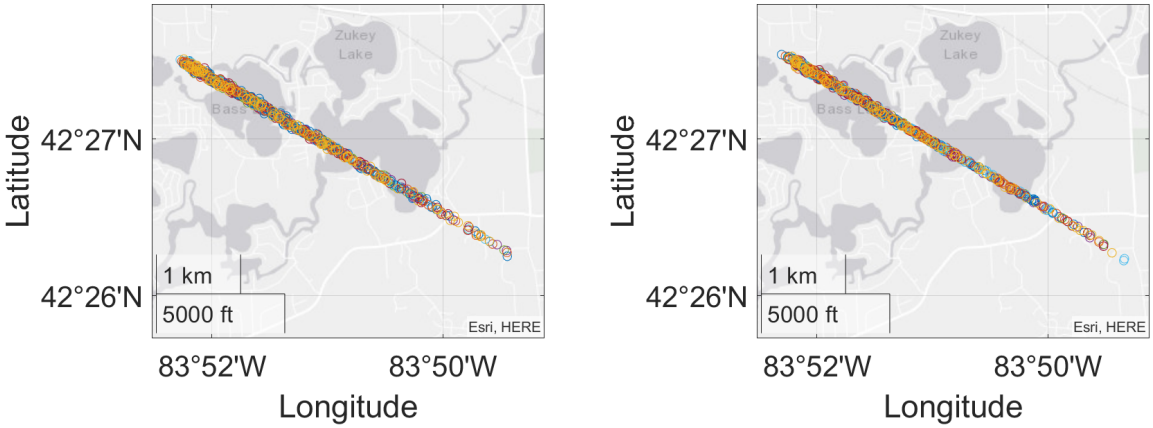

(a) Wind file at 00:00.

(b) Wind file at 06:00.

Figure 59: Impact coordinates for the two different wind file times.

8 Conclusions and future work

8.1 Conclusions

After the realization of this project it can be said that the initial objectives have been fulfilled. On one hand, a numerical code has been developed capable of simulating the trajectory of meteoroids in the Earth's atmosphere and calculating the impact coordinates of meteorite fragments with the ground and on the other hand, a code has been developed to calculate the heliocentric orbits of the meteoroids before they are affected by the Earth's gravity. Both programs offer relatively accurate results for the chosen case of study, the Hamburg meteorite.

As discussed throughout the report, the trajectory model depends on many parameters that are uncertain, in the sense that it is very difficult to determine them from the meteorite recordings alone. Within these parameters, studied individually in the sensitivity study, those that have the most important effect on the number, size and location of the meteorite fragments are those related to the fragmentation model and the wind model. Moreover, it is precisely in these models that the greatest sources of error are found.

The first clear divergence with the recovered data is that the assumed fragmentation model generates an unrealistic amount of fragments and, although these are similar in size to those recovered, the number is too large. In the sensitivity study, it has been seen that a model with more freedom of mass distribution, where a higher percentage of dust mass is generated in each fragmentation event, is more suitable for this case of study, as the number of fragments is reduced to plausible numbers without changing the sizes and locations of the meteorite fragments. The other parameters related to fragmentation, however, varied both the number and size of fragments at the same time, so that if the number of fragments decreased, their size increased. However, in order to decide with more certainty which model best reflects reality, other meteorites with different properties should be studied.

The second main divergence is that the average trajectory line of the fragments differs a bit from the one of the recovered meteorites. This error affects more the fragments with less mass, while the larger fragments appear closer to their corresponding location based on the recovered meteorites. As seen in the sensitivity study, the only parameter affecting the average

trajectory line is the wind. That is why, to get more accurate results, it is necessary to find a wind model that is more precise. The current model can only give a qualitative idea of the wind direction and speed.

On the results of the orbit calculation, the orbital elements obtained with the developed model don't exactly match the ones obtained in the article that studied this meteorite. That is because the procedure for obtaining the initial heliocentric speeds and positions is not the same. Even so, the orbit obtained is very similar, having the same eccentricity and semi-major axis, but with slightly different orbital orientation angles.

In conclusion, the numerical code developed in this thesis meets the requirements imposed in the introduction, offering results with a precision considered acceptable, since both the meteorite coordinates and their size are very similar to those recovered, and it is considered that they could be found based on them (the coordinates of the meteorites recovered are no more than 500 m radius of distance from the simulation results). Finally, in order to adjust and improve the accuracy, the model should be tested with other meteorite falls and with a more precise wind model specific for each case.

8.2 Future work

This section will discuss possible improvements that could be made to improve the performance and accuracy of the model.

Firstly, the model should be tested with several meteorite falls of different physical properties and, based on that, the distribution of mass after each breakup should be chosen.

Secondly, the wind model should be improved, either by choosing a more local wind model or by developing a more precise global model.

Thirdly, the code that calculates the heliocentric orbit of the meteoroid should be validated and the assumption that the Earth's gravity does not affect the orbit significantly should be demonstrated.

Fourthly, the code should be optimized in order to reduce the time of simulation, which at the moment is quite long (several minutes per simulation), and eventually changed to a more

efficient programming language, such as C.

Finally, given the large number of uncertain parameters that exist in the problem, it would be interesting to develop a Monte Carlo algorithm around this model to see if there exists deterministic result resulting from the combination of different parameter values that is accurate.

References

[1] *Meteorite Importance | Center for Meteorite Studies | ASU*. URL: https://meteorites.asu.edu/meteorites/importance-of-meteorites (visited on 10/22/2019).

[2] *Learning from Meteorites: 4.6 Billion Years of History | AMNH*. URL: https://www.amnh.org/exhibitions/permanent/meteorites/meteorites/what-is-a-meteorite/history (visited on 10/22/2019).

[3] Paul J. Register, Donovan L. Mathias, and Lorien F. Wheeler. "Asteroid fragmentation approaches for modeling atmospheric energy deposition". In: *Icarus* 284 (2017), pp. 157–166. ISSN: 10902643. DOI: 10.1016/j.icarus.2016.11.020. URL: http://dx.doi.org/10.1016/j.icarus.2016.11.020.

[4] P M Mehta, E Minisci, and M Vasile. "Break-up modelling and trajectory simulation under uncertainty for asteroids". In: *Proceeding of the 4th IAA Planetary Defense Conference, Frascati, Roma* July (2015), pp. 13–17.

[5] IAU. *Meteors & Meteorites: The IAU Definitions of Meteor Terms | IAU*. URL: https://www.iau.org/public/themes/meteors{_}and{_}meteorites/ (visited on 11/13/2019).

[6] Zdeň Ek Ceplecha, Jiří Jiˇ, Jiří Borovička, Boroviˇ Borovička, W Graham Elford, Douglas O Revelle, and Robert L Hawkes. "Meteor Phenomena and Bodies". In: *Space Science Reviews* 84.3-4 (1998), pp. 327–471.

[7] NASA. "Glossary". In: (2019).

[8] V. A. Bronshten. *Physics of Meteoric Phenomena*. Springer Netherlands, 1983, p. 380. ISBN: 9789400972247.

[9] *Meteor Crater: Arizona's other huge hole in the ground*. URL: https://eu.azcentral.com/story/travel/arizona/road-trips/2017/10/17/meteor-crater-arizona/541387001/ (visited on 01/14/2020).

[10] Kerry Lotzof. *Types of meteorites | Natural History Museum*. 2018. URL: https://www.nhm.ac.uk/discover/types-of-meteorites.html (visited on 11/22/2019).

[11] Geoffrey Notkin. *Types of Meteorites: Iron, Stone, Stony-Iron, Lunar, Martian*. URL: https://geology.com/meteorites/meteorite-types-and-classification.shtml (visited on 11/22/2019).

[12] Jiří Borovička. "Physical and chemical properties of meteoroids as deduced from observations". In: *International Astronomical Union* (2005). DOI: 10.1017/S1743921305006782.

[13] Zdeněk Ceplecha and Douglas O. ReVelle. "Fragmentation model of meteoroid motion, mass loss, and radiation in the atmosphere". In: *Meteoritics and Planetary Science* 40.1 (2005), pp. 35–54. ISSN: 10869379. DOI: 10.1111/j.1945-5100.2005.tb00363.x.

[14] Z. Ceplecha. "Multiple fall of Přibram meteorites photographed. 1. Double-station photographs of the fireball and their relations to the found meteorites". In: *Bulletin of the Astronomical Institutes of Czechoslovakia* 12 (1961), p. 21.

[15] J. Borovička, P. Spurný, D. Šegon, Andreić, J. Kac, K. Korlević, J. Atanackov, G. Kladnik, H. Mucke, D. Vida, and F. Novoselnik. "The instrumentally recorded fall of the Križevci meteorite, Croatia, February 4, 2011". In: *Meteoritics and Planetary Science* 50.7 (2015), pp. 1244–1259. ISSN: 10869379. DOI: 10.1111/maps.12469.

[16] *Benchmarks: January 3, 1970: Lost City meteorite is tracked and recovered | EARTH Magazine*. URL: https://www.earthmagazine.org/article/benchmarks-january-3-1970-lost-city-meteorite-tracked-and-recovered (visited on 10/22/2019).

[17] R. E. McCrosky, A. Posen, G. Schwartz, and C.-Y. Shao. "Lost City meteorite-Its recovery and a comparison with other fireballs". In: *Journal of Geophysical Research* 76.17 (1971), pp. 4090–4108. ISSN: 0148-0227. DOI: 10.1029/jb076i017p04090. URL: http://doi.wiley.com/10.1029/JB076i017p04090.

[18] I. Halliday, A. T. Blackwell, A. A. Griffin, I. Halliday, A. T. Blackwell, and A. A. Griffin. "The Innisfree Meteorite and the Canadian Camera Network". In: *Journal of the Royal Astronomical Society of Canada* 72 (1978), p. 15. URL: https://ui.adsabs.harvard.edu/abs/1978JRASC..72...15H/abstract.

[19] Olga Popova. *Meteoroid ablation models*. 2004. DOI: 10.1007/s11038-005-9026-x.

[20] *ECEF - Wikipedia*. URL: https://en.wikipedia.org/wiki/ECEF{\#}/media/File:Ecef.png (visited on 12/04/2019).

[21] M. M. Macomber. "World geodetic system, 1984." In: (1984).

[22] Barry Kronenfeld. "GIS Fundamentals: A First Text o Geographic Information Systems (2nd edition)". In: *Photogrammetric engineering and remote sensing* 72.10 (2006), p. 1119. ISSN: 0099-1112. URL: http://www.paulbolstad.net/5thedition/samplechaps/Chapter3{_}5th{_}small.pdf.

[23] L. D. Landau and E. M. Lifshitz. *Mechanics*. Pergamon Press, 1960, pp. 4–6.

[24] Zornoza Hernández and M. *Conventional Celestial Reference System - Navipedia*. URL: https://gssc.esa.int/navipedia/index.php/Conventional{_}Celestial{_}Reference{_}System (visited on 12/04/2019).

[25] Inc. The MathWorks. *Convert Earth-centered Earth-fixed (ECEF) coordinates to geodetic coordinates*. 2014. URL: https://es.mathworks.com/help/aerotbx/ug/ecef2lla.html (visited on 10/09/2019).

[26] *Introduction to SPICE*. 2014. URL: https://naif.jpl.nasa.gov/pub/naif/toolkit{_}docs/C/info/intrdctn.html (visited on 01/04/2020).

[27] Ferdinand P. (Ferdinand Pierre) Beer, E. Russell. Johnston, and Phillip J. Cornwell. *Mecanica vectorial para ingenieros : dinamica*. McGraw-Hill, 2010. ISBN: 9786071502612.

[28] James T. Cushing and James T. Cushing. "Newton's law of universal gravitation". In: *Philosophical Concepts in Physics*. 2012, pp. 103–113. DOI: 10.1017/cbo9781139171106.012.

[29] D McKinley. *Meteor science and engineering*. New York: mckinley, 1961. URL: https://www.worldcat.org/title/meteor-science-and-engineering/oclc/489909673.

[30] P. G. Brown, D. Vida, D. E. Moser, M. Granvik, W. J. Koshak, D. Chu, J. Steckloff, A. Licata, S. Hariri, J. Mason, M. Mazur, W. Cooke, and Z. Krzeminski. "The Hamburg meteorite fall: Fireball trajectory, orbit, and dynamics". In: *Meteoritics and Planetary Science* 54.9 (2019), pp. 2027–2045. ISSN: 10869379. DOI: 10.1111/maps.13368.

[31] Elizabeth A. Silber, Mark Boslough, Wayne K. Hocking, Maria Gritsevich, and Rodney W. Whitaker. "Physics of meteor generated shock waves in the Earth's atmosphere – A review". In: *Advances in Space Research* 62.3 (2018), pp. 489–532. ISSN: 18791948. DOI: 10.1016/j.asr.2018.05.010. URL: https://doi.org/10.1016/j.asr.2018.05.010.

[32] National Geophysical Data Center. *U.S. standard atmosphere (1976)*. 1992. DOI: 10.1016/0032-0633(92)90203-Z.

[33] *Use 1976 COESA model - MATLAB atmoscoesa - MathWorks España*. URL: https://es.mathworks.com/help/aerotbx/ug/atmoscoesa.html (visited on 01/05/2020).

[34] *Use International Standard Atmosphere model - MATLAB atmosisa*. URL: https://www.mathworks.com/help/aerotbx/ug/atmosisa.html (visited on 01/07/2020).

[35] *Empirical Modeling of the Upper Atmosphere: NRLMSISE-00, HWM07, and G2S | Space Science Division*. URL: https://www.nrl.navy.mil/ssd/branches/7630/modeling-upper-atmosphere (visited on 12/09/2019).

[36] *Implement mathematical representation of 2001 United States Naval Research Laboratory Mass Spectrometer and Incoherent Scatter Radar Exosphere - MATLAB atmosnrlmsise00 - MathWorks España*. URL: https://es.mathworks.com/help/aerotbx/ug/atmosnrlmsise00.html (visited on 12/24/2019).

[37] *Global Forecast System (GFS) | National Centers for Environmental Information (NCEI) formerly known as National Climatic Data Center (NCDC)*. URL: https://www.ncdc.noaa.gov/data-access/model-data/model-datasets/global-forcast-system-gfs (visited on 12/16/2019).

[38] J. G. Hills and M. P. Goda. "The fragmentation of small asteroids in the atmosphere". In: *The Astronomical Journal* 105 (1993), p. 1114. ISSN: 00046256. DOI: 10.1086/116499.

[39] Douglas O. ReVelle, Revelle, and Douglas O. "NEO fireball diversity: energetics-based entry modeling and analysis techniques". In: *Proceedings of the International Astronomical Union* 2.S236 (2006), pp. 95–106. ISSN: 17439213. DOI: 10.1017/S1743921307003122. URL: https://www.cambridge.org/core/product/identifier/S1743921307003122/type/journal{_}articlehttp://articles.adsabs.harvard.edu/cgi-bin/nph-iarticle{_}query?2007IAUS..236...95R{\&}defaultprint=YES{\&}filetype=.pdf.

[40] Lorien F Wheeler, Paul J Register, and Donovan L Mathias. "A fragment-cloud model for asteroid breakup and atmospheric energy deposition". In: *Icarus* 295 (2017), pp. 149–169. ISSN: 10902643. DOI: 10.1016/j.icarus.2017.02.011.

[41] Philip A. Bland and Natalya A. Artemieva. "The rate of small impacts on Earth". In: *Meteoritics and Planetary Science* 41.4 (2006), pp. 607–631. ISSN: 10869379. DOI: 10.1111/j.1945-5100.2006.tb00485.x.

[42] Quinn R. Passey and H. J. Melosh. "Effects of atmospheric breakup on crater field formation". In: *Icarus* 42.2 (1980), pp. 211–233. ISSN: 10902643. DOI: 10.1016/0019-1035(80)90072-X.

[43] S. J. Laurence and R. Deiterding. "Shock-wave surfing". In: *Journal of Fluid Mechanics* 676.12 (2011), pp. 396–431. ISSN: 14697645. DOI: 10.1017/jfm.2011.57.

[44] S. J. Laurence, N. J. Parziale, and R. Deiterding. "Dynamical separation of spherical bodies in supersonic flow". In: *Journal of Fluid Mechanics* 713 (2012), pp. 159–182. ISSN: 00221120. DOI: 10.1017/jfm.2012.453.

[45] Josep M. Trigo-Rodríguez, Jiří Borovička, Pavel Spurný, José L. Ortiz, José A. Docobo, Alberto J. Castro-Tirado, and Jordi Llorca. "The Villalbeto de la Peña meteorite fall: II. Determination of atmospheric trajectory and orbit". In: *Meteoritics and Planetary Science* 41.4 (2006), pp. 505–517. ISSN: 10869379. DOI: 10.1111/j.1945-5100.2006.tb00478.x.

[46] Jiří Borovička, Juraj Tóth, Antal Igaz, Pavel Spurný, Pavel Kalenda, Jakub Haloda, Ján Svoreň, Leonard Kornoš, Elizabeth Silber, Peter Brown, and Marek Husárik. "The Košice meteorite fall: Atmospheric trajectory, fragmentation, and orbit". In: *Meteoritics and Planetary Science* 48.10 (2013), pp. 1757–1779. ISSN: 10869379. DOI: 10.1111/maps.12078.

[47] Ana Laura Zabala López. "ANÁLISIS Y DESARROLLO DE ALGORITMOS PARA LA PLANIFICACIÓN OPTIMIZADA DE ADQUISICIÓN DE IMÁGENES TERRESTRES". PhD thesis. Universidad de Sevilla, 2013. URL: http://bibing.us.es/proyectos/abreproy/60221.

[48] Howard D. Curtis. *Orbital Mechanics for Engineering Students*. Elsevier Science & Technology, 2019, p. 964. ISBN: 9780081021347.

[49] Yuchul Shin, Seyoung Yoon, Yongmyung Seo, Ho Jin, and Jongho Seon. "Radiation effect for a CubeSat in slow transition from the Earth to the Moon". In: *Advances in Space Research* 55.7 (2015), pp. 1792–1798. ISSN: 18791948. DOI: 10.1016/j.asr.2015.01.018.

[50] Z Ceplecha. "Geometric, dynamic, orbital and photometric data on meteoroids from photographic fireball networks". In: *Astronomical Institutes of Czechoslovakia* 38 (1987), p. 222. URL: http://adsabs.harvard.edu/cgi-bin/nph-data{_}query?bibcode=1987BAICz..38..222C{\&}link{_}type=ABSTRACT{\%}5Cnpapers://28ddb9e4-2f98-4aa9-b14d-eceaaf9fa142/Paper/p133.

[51] Inc. The MathWorks. *Resolver ecuaciones diferenciales no rígidas: método de orden medio - MATLAB ode45 - MathWorks América Latina*. 2019. URL:

https://es.mathworks.com/help/matlab/ref/ode45.htmlhttps://la.mathworks.com/help/matlab/ref/ode45.html (visited on 10/09/2019).

[52] *Create or modify options structure for ODE and PDE solvers - MATLAB odeset - MathWorks España*. URL: https://es.mathworks.com/help/matlab/ref/odeset.html (visited on 12/24/2019).

[53] V. V. Svetsov, I. V. Nemtchinov, and A. V. Teterev. "Disintegration of Large Meteoroids in Earth's Atmosphere: Theoretical Models". In: *Icarus* 116.1 (1995), pp. 131–153. ISSN: 00191035. DOI: 10.1006/icar.1995.1116.

[54] Clemens Rumpf, Hugh G Lewis, and Peter M Atkinson. "On the influence of impact effect modelling for global asteroid impact risk distribution". In: (2016). DOI: 10.1016/j.actaastro.2016.03.015. URL: http://dx.doi.org/10.1016/j.actaastro.2016.03.015.